Biomaterials Advances 188 (2026) 215007

Contents lists available at ScienceDirect

Biomaterials Advances

journal homepage: www.journals.elsevier.com/materials-science-and-engineering-c

Biodegradable nano-dental-chip of nutraceuticals as a local drug delivery system for periodontal pockets

Rabia Ashfaq [a], Anita Kovács [a], Szilvia Berkó [a], Gábor Katona [a], Rita Ambrus [a], Tamás F. Polgár [b,c], Mária Szécsényi [d], Katalin Burián [d], Mária Budai-Szűcs [a,*]

[a] Institute of Pharmaceutical Technology and Regulatory Affairs, Faculty of Pharmacy, University of Szeged, H-6720, Szeged, Hungary
[b] Core Facility, HUN-REN Biological Research Centre, H-6726, Szeged, Hungary
[c] HUN-REN-SZTE Neuroscience Research Group, Hungarian Research Network, University of Szeged, H-6725, Hungary
[d] Department of Medical Microbiology, University of Szeged, H-6720, Szeged, Hungary

ARTICLE INFO

Keywords:
Clove oil
Apigenin
SEM
Biopolymer film
Dental chip
Periodontal cavity

ABSTRACT

Periodontal infections continue to pose a significant clinical challenge, primarily due to the limited residence time of conventional formulations within periodontal pockets and the consequent need for repeated administration. The present study aimed to develop a biodegradable, mucoadhesive nano-dental-chip as a localized antibacterial delivery platform for sustained periodontal therapy. Nanostructured lipid carriers (NLC) incorporating clove oil (CO) and apigenin (AP) were prepared and characterized for particle size, polydispersity index, zeta potential, and entrapment efficiency. Optimized NLC exhibited nanoscale dimensions (160–188 nm), narrow size distribution (PDI < 0.30), and high drug entrapment (>94%). Nanocarriers were incorporated into biodegradable polymeric films composed of gelatin (GEL) blended with either chitosan (CH) or carboxymethylcellulose (CMC), which were subsequently fabricated into periodontal chips *via* the solvent casting method. Comprehensive physicochemical, mechanical, and mucoadhesive evaluations demonstrated uniform thickness, acceptable surface pH (5.5–7.0), low moisture content (<2%), high resilience, and adequate burst strength. Molecular docking studies revealed thermodynamically favorable interactions between polymers and bioactive compounds, supporting effective drug stabilization. Consistent with the sustained release profiles of eugenol and AP, zone of inhibition and time-kill assays revealed potent antibacterial activity, culminating in the complete eradication of *Aggregatibacter actinomycetemcomitans* and prolonged growth suppression of *Streptococcus mutans*. Stability studies further indicated preservation of physicochemical properties under various storage conditions. These findings highlight the nano-dental chip as a promising biodegradable, site-specific delivery system capable of sustained retention, controlled drug release, and enhanced antibacterial efficacy for periodontal infection treatment.

1. Introduction

Human dental plaque consists of a diverse and fully metabolically integrated community of microorganisms that forms a complex biofilm, playing a critical role in both oral health and disease [1]. The primary cause of periodontitis is a disruption in the balance between the host's immune response and the microbial biofilm, which triggers inflammation and tissue destruction. This inflammatory process damages the gums, bone, and connective tissues, ultimately resulting in broader dental abnormalities and irreversible tooth loss. Most localized or progressive orodental infections develop when microorganisms from dental plaque infiltrate the surrounding oral tissues. Plaque accumulates in the pits and fissures of teeth adjacent to the gingival margin, leading to gingival inflammation [2]. In addition, supragingival plaque is a primary factor in the development of dental caries, whereas subgingival plaque is predominantly responsible for periodontal disease [3]. Among the microorganisms residing within the plaque, several bacterial species have been identified as causative agents of periodontitis, including *Porphyromonas gingivalis*, *Treponema denticola*, *Tannerella forsythia*, *Aggregatibacter actinomycetemcomitans*, *Fusobacterium nucleatum*, *Prevotella intermedia*, and *Campylobacter rectus* [4]. Such microbial involvement presents a significant challenge in biomedical applications,

* Corresponding author.
E-mail address: budai-szucs.maria@szte.hu (M. Budai-Szűcs).

https://doi.org/10.1016/j.bioadv.2026.215007
Received 23 March 2026; Received in revised form 4 June 2026; Accepted 8 June 2026
Available online 9 June 2026

particularly in tissue-related conditions where bacterial colonization can hinder therapeutic success. Moreover, the growing prevalence of bacterial infections places a substantial burden on healthcare systems, underscoring the urgent need for more effective treatment strategies [5,6].

Conventional treatment approaches rely on antibacterial agents such as antibiotics or antimicrobial compounds as adjunct therapies to control bacterial proliferation. However, prolonged or excessive use of antibiotics may contribute to the development of resistance in oral pathogens, resulting in recurrent bacterial colonization [7].

Furthermore, the effective management of localized periodontal infections remains a clinical challenge due to the limited residence time of conventional formulations within the periodontal pocket and the need for frequent drug administration. Systemic delivery often results in subtherapeutic concentrations at the target site while increasing the risk of adverse effects [6].

Biomaterials are sustainable, bio-derived materials originating from natural biological systems, extensively employed across pharmaceutical and food science disciplines for a wide range of applications [8]. Their growing prominence is primarily attributed to their superior biocompatibility with physiological environments and their inherent biodegradability, which enables safe and efficient integration as well as natural degradation without inducing adverse effects [9].

Gelatin (GEL) is the partially hydrolyzed form of collagen, which offers exceptional biocompatibility, biodegradability, non-toxicity, and cost-effectiveness, making it a popular choice as a film-forming biopolymer. Thin, flexible, and translucent GEL films are particularly useful for carrying or immobilizing additives that enhance their functional properties [10]. However, the use of GEL in various applications can be limited by its strong moisture absorption (water vapor permeability) and relatively low mechanical and thermal strength. A practical approach to enhance the physical characteristics of GEL films is to blend them with other biopolymers [11,12].

Polysaccharides are widely recognized as cost-effective and readily available raw materials for producing biodegradable films. The abundance of polar groups, particularly hydroxyl groups, along their polymer chains enables polysaccharides to form extensive hydrogen bonding networks, which are essential for their film-forming abilities [12]. Polysaccharide-based films typically exhibit excellent barrier properties against gases like oxygen and carbon dioxide, although their hydrophilic nature results in relatively poor resistance to water vapor [13].

Interactions between proteins and polysaccharides of different origins can be harnessed to create materials with customized functional properties. The formation and behavior of these complexes are influenced by multiple factors, including the composition, concentration, and ratios of the components; the sequence in which they are mixed; the pH and charge distribution; the molecular weight; and the conformation of the polymers. Additionally, the ionic strength of the solution and the type of ions present play a significant role in determining the nature and stability of the complexes [14]. In the biopolymer-rich phase, proteins and polysaccharides are primarily associated through electrostatic interactions, forming structures such as coacervates, soluble or insoluble complexes, and gels [15].

Cellulose is a linear polysaccharide made of glucose units linked by β-1,4 glycosidic bonds. The presence of hydroxyl groups per glucose unit enables cellulose to react with various reagents, yielding numerous derivatives. As a Generally Recognized as Safe (GRAS) substance, cellulose's properties, such as solubility, water affinity, crystallinity, and film-forming ability, can be modified through different chemical processes. For example, cellulose undergoes esterification with carboxymethyl groups to produce carboxymethyl cellulose (CMC) esters [16]. CMC, an anionic derivative of cellulose, contains multiple hydrophilic carboxyl groups attached to its hydrophobic backbone, giving it distinct amphiphilic properties [17]. It is a widely used cellulose ether derivative in food applications due to its thickening, gelling, stabilizing, emulsifying, and bulking properties. CMC is also popular for its viscosity, flocculation, transparency, non-toxicity, non-allergenicity, and affordability [18].

It holds GRAS status from the FDA (FDA, 1973) and can also be used to create biodegradable films due to its high molecular weight and polymer structure [19,20]. The literature mentioned that films produced from CMC exhibit enhanced mechanical properties. Its high water affinity allows CMC to form strong, flexible, and self-supporting films on its own [21,22].

Chitosan (CH) has emerged as one of the most promising biopolymers in recent years due to its biocompatibility, biodegradability, non-toxicity, broad-spectrum antimicrobial, antioxidant, and antitumor properties [23,24]. Additionally, it is a cost-effective material, primarily sourced from marine waste, such as seafood shells. Chitin, a naturally occurring mucopolysaccharide found in the exoskeletons of insects and crustaceans, serves as the precursor to CH, which is obtained through an alkaline deacetylation process [25,26].

The chemical structure of CH comprises both deacetylated and acetylated segments, namely, D-glucosamine and *N*-acetyl-D-glucosamine, linked together by 1,4-glycosidic bonds [27]. CH is a cationic biopolymer that carries a positive charge and becomes soluble in acidic conditions (below pH 6.5) due to the protonation of its amino groups. This cationic nature enables CH to form electrostatic interactions with various compounds, allowing it to be processed into different forms such as edible films, gels, and nanoparticles, and making it widely applicable in food packaging and other functional material developments [28,29]. CH has become increasingly valuable in the pharmaceutical industry due to its biodegradability and minimal toxicity. It has shown significant potential in wound healing applications owing to its ability to promote tissue regeneration and inhibit bacterial infections [30]. These properties are particularly advantageous in environments where both tissue repair and infection control are critical. Additionally, CH's physicochemical characteristics make it an ideal candidate for drug delivery systems and tissue engineering applications, where it serves as an effective matrix material for therapeutic delivery [31]. Its remarkable film-forming capability further supports its application as a packaging material by imparting favorable mechanical strength and barrier properties to films [32].

Generally, films made from CH/GEL blends exhibit superior mechanical strength and barrier properties compared with those composed of CH or GEL individually [33,34]. Research has shown that GEL and CH interact primarily through electrostatic and intermolecular hydrogen bonding [35]. The electrostatic interactions primarily arise between the positively charged amino groups of CH and the negatively charged carboxyl groups of GEL, while hydrogen bonds form both within and between the polymer chains through the involvement of hydroxyl, carbonyl, and amino groups. These strong intermolecular forces contribute to the formation of diverse complex structures between the two biopolymers [11].

Existing periodontal chips and films reported in the literature, such as chlorhexidine-loaded chips [36], ciprofloxacin dental film [37], tetracycline fibers [38], and minocycline-based local delivery systems [39] have been primarily designed to deliver a single antiseptic or antibiotic agent for localized antimicrobial action. However, these systems typically lack the complementary anti-inflammatory and antioxidant activities that are highly desirable for managing the complex pathophysiology of periodontal disease.

On the other side, the growing prevalence of antibiotic resistance, along with the adverse effects associated with long-term antibiotic therapy, has stimulated increasing interest in plant-derived bioactives as safer and sustainable alternatives for disease management [40]. Clove oil (CO) contains numerous bioactive constituents, among which eugenol (Eug) is the most abundant component. The phenolic group of Eug exhibits strong antioxidant, antibacterial, antiviral, antifungal, anticancer, antimutagenic, antiallergic, anti-inflammatory, and analgesic activities [41]. The concentration of Eug in CO varies depending on the genetic origin of the clove tree, geographical growing conditions,

the plant part used, and the method of extraction [42]. Apigenin (AP) (4′,5,7-trihydroxyflavone) is a plant-derived flavonoid abundantly present in fruits, vegetables, nuts, and herbs, and it exhibits diverse biological activities, including antimicrobial, antidiabetic, antioxidant, anti-inflammatory, and anticancer properties [43,44].

Nanostructured lipid carriers (NLC) have emerged as a promising lipid-based nanocarrier system due to their high drug loading capacity, controlled release behavior, and improved stability compared to conventional drug delivery systems [45,46]. Consistent with these, our already optimized NLC formulation incorporating CO (Eug) as the therapeutic liquid lipid, together with AP as the active agent, exhibited notable antibacterial, antioxidant, and anti-inflammatory activities, highlighting its potential as a promising substitute for conventional antibiotics [47]. However, the direct clinical translation of such nanocarriers is limited by their rapid clearance from the periodontal site when administered alone. To overcome this limitation, the present study adopts a promising strategy by integrating the optimized NLC into a biodegradable polymeric periodontal chip composed of GEL with CH or CMC, thereby enhancing local retention and enabling controlled drug delivery. Molecular docking studies were first employed to elucidate drug–polymer interactions, providing mechanistic insights into matrix stabilization and release behavior through the assessment of binding affinities between phytoconstituents and biomaterials. The developed system was subsequently evaluated through comprehensive physicochemical, mechanical, and antibacterial investigations against key periodontal pathogens. This integrated approach, combining nanoscale drug encapsulation with a biodegradable polymeric matrix, offers prolonged therapeutic activity, enhanced mucoadhesion, and matrix-mediated controlled drug release while eliminating the need for surgical retrieval. Collectively, these attributes position the proposed nanodental chip as a promising site-specific delivery system for sustained periodontal therapy.

2. Materials and method

2.1. Materials

Compritol® 888 ATO (glycerol dibehenate; S.L (as solid lipid)), clove essential oil (CO, derived from Eugenia species, containing 76.8% eugenol; Eug), and Kolliphor® RH40 (PEG-40 hydrogenated castor oil; KRH40) were procured from Gattefossé (Saint-Priest Cedex, France), Sigma-Aldrich (Steinheim, Germany), and BASF SE Chemtrade GmbH (Ludwigshafen, Germany), respectively. Apigenin (AP; purity >94% sourced from Biosynth s.r.o. (Bratislava, Slovakia). Gelatin (GEL: gel strength 225 g Bloom, Type B: Bovine gelatin) and Chitosan (CH: low molecular weight) were purchased from Sigma-Aldrich (St. Louis, MO, USA). Carboxymethylcellulose (CMC: Blanose®) was supplied by Ashland Global Holdings Inc., Delaware, USA. Glycerol 87% and mucin (8% v/v; porcine gastric, grade III) were obtained from Sigma-Aldrich Co. Ltd. (Budapest, Hungary). Acetonitrile (AcN), glacial acetic acid (GAA), methanol, and 96% ethanol were purchased from VWR International (Debrecen, Hungary). Purified water from Millipore Milli-Q® 140 Gradient system (Merck Ltd., Budapest, Hungary) was used for all aqueous preparations. All chemicals and materials used were of analytical grade.

2.2. Preliminary study

Polymer film-forming solutions were prepared using CH (3% w/w), CMC (3% w/w), and GEL (6% w/w) as mentioned in Section 2.8. These solutions were blended in two different CMC/CH-to-GEL ratios: 50:50 and 25:75 (w/w). Glycerol was incorporated as a plasticizer at two levels, 30% and 40% (w/w), equivalent to the total polymer content. The resulting polymer dispersions were cast into glass petri dishes and allowed to dry at ambient temperature. Upon complete drying, the films were cut into uniform pieces and subjected to preliminary screening tests to assess their physical integrity for further nanoloading. Comprehensive data for all film formulations, including composition and initial screening outcomes, are provided in the Supplementary material (Table S1).

Based on their superior % resilience, mucoadhesive and surface characteristics, the 50:50 polymer ratio combined with 40% glycerol concentration was selected as the optimal composition for further nanoparticle loading and formulation development.

2.3. Preparation of NLC

NLC is prepared using a probe ultrasonication method, as previously published [47]. The lipid phase, consisting of 4.57% S.L, AP (250 μg/mL, 500 μg/mL), and 3.57% surfactant (KRH40), was first heated to 85 °C, approximately 10 °C above the melting point of the solid lipid, to ensure complete melting. Later, the 1.5% liquid lipid (CO) was incorporated into the molten mixture (Table 1). In parallel, the aqueous phase was heated to the same temperature and then gradually introduced into the lipid phase under continuous stirring to produce a coarse pre-emulsion. This mixture was subsequently subjected to ultrasonication using a Hielscher UP200S ultrasonic homogenizer (Hielscher Ultrasonics GmbH, Germany) at 70% amplitude for 5 min to reduce particle size and generate nanoscale lipid droplets (Scheme 1a). The resulting dispersion was immediately cooled in an ice bath to solidify the lipid matrix and stabilize the nanocarriers. The final NLC dispersion was transferred into airtight containers and stored in a refrigerator until further use.

2.4. Dynamic light scattering (DLS) measurement

The average particle size (Z_{ave}), polydispersity index (PDI), and zeta potential (ZP) of NLC formulations were characterized using DLS at a wavelength of 633 nm, employing a Zetasizer Nano ZS instrument (Malvern Instruments, Worcestershire, UK). For each measurement, samples were diluted tenfold with deionized water and loaded into DTS 1070 folded capillary cells. Measurements were conducted at 25 °C with an integration time of 110 s to ensure accuracy and reproducibility. Results are recorded in average with standard deviation (±SD).

2.5. Entrapment efficiency (EE) of nanoparticles

To separate unencapsulated Eug and AP from the nanocarrier dispersions, ultrafiltration was carried out using Vivaspin 15R centrifugal concentrators with a 5 kDa molecular weight cut-off (Hydrosart membrane; Sartorius, Stonehouse, UK). Samples were centrifuged at 14,000 rpm (approximately 9000 ×g) for 40 min at 5 °C in a Hermle Z323K high-speed refrigerated centrifuge (HERMLE Labortechnik GmbH, Wehingen, Germany). The process yielded a transparent aqueous layer with the free, unencapsulated Eug and AP, which was subsequently quantified using High-Performance Liquid Chromatography (HPLC) as described in Section 2.16. The EE% was then determined indirectly using the following Eq. (1).

$$EE\% = \frac{W_{loaded\ drug} - W_{free\ drug}}{W_{loaded\ drug}} \times 100 \quad (1)$$

2.6. Morphological analysis (transmission electron microscopy (TEM))

The morphology and distribution of nanoformulations were examined using a JEM-1400 Flash transmission electron microscope (JEOL, Tokyo, Japan). For sample preparation, 100 times diluted 10 μL of nanodispersion was applied onto a formvar-coated 150-mesh copper grid (Electron Microscopy Sciences, Hatfield, PA, USA). After 1 min of setting time, any excess liquid was gently removed with filter paper. The grids were then negatively stained twice with 10 μL of 2% uranyl acetate (Electron Microscopy Sciences, Hatfield, PA, USA) prepared in Millipore

Table 1
Composition of NLC and corresponding polymeric-loaded and blank films.

Formulations	Solid lipid (%)	Liquid lipid (%)	Surfactant (%)	Apigenin (μg/mL)	CMC (%)	CH (%)	GEL (%)
NLC-A	4.57	1.50	3.57	250	–	–	–
NLC-B	4.57	1.50	3.57	500	–	–	–
GC40-A	4.57	1.50	3.57	250	3	–	6
GC40-B	4.57	1.50	3.57	500	3	–	6
GH40-A	4.57	1.50	3.57	250	–	3	6
GH40-B	4.57	1.50	3.57	500	–	3	6
GC40	–	–	–	–	3	–	6
GH40	–	–	–	–	–	3	6

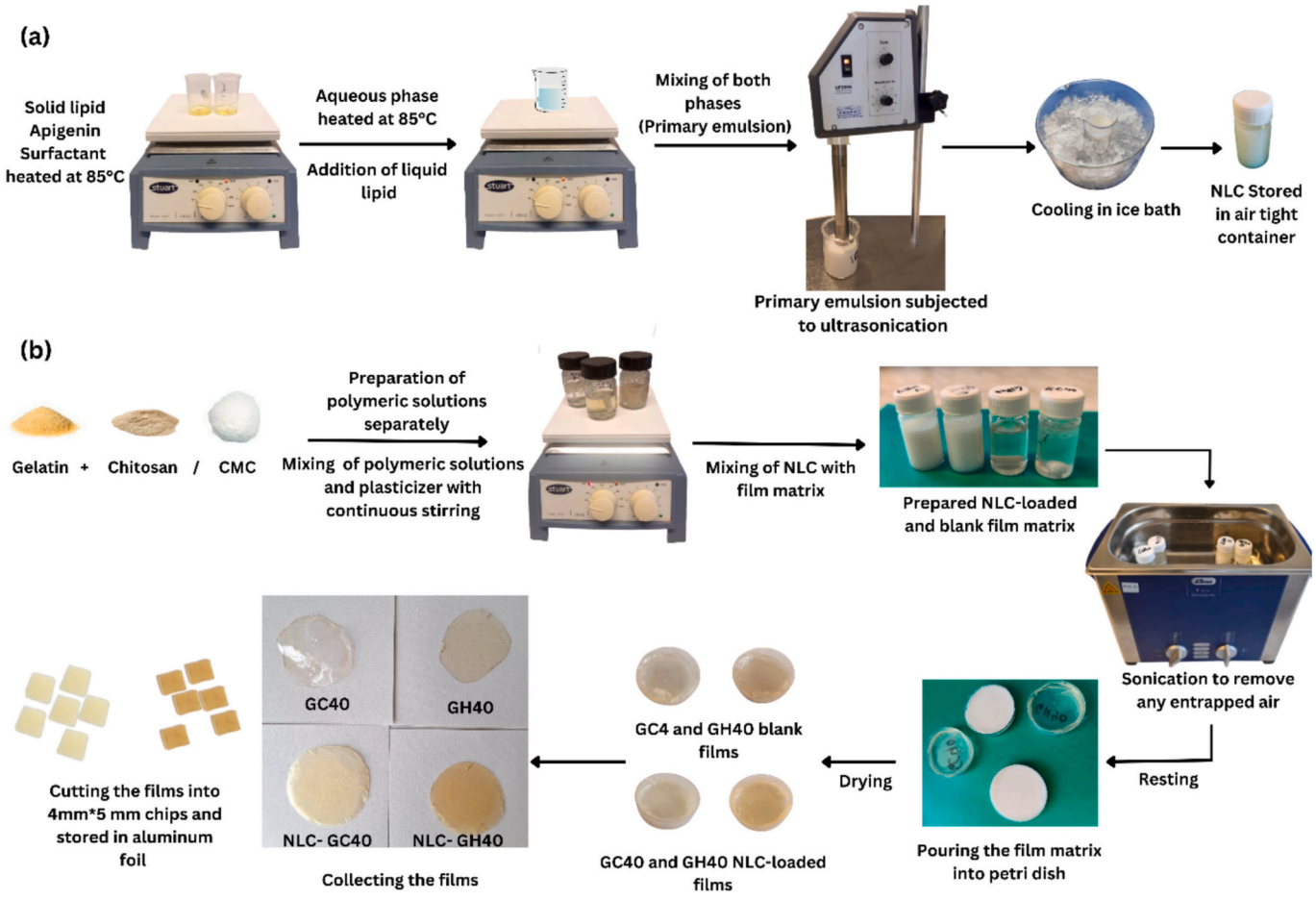

Scheme 1. Method of preparation of NLC (a) and fabrication of blank and NLC-loaded films and obtaining of dental chips (b).

water for 2 min. Excess staining solution was removed, and the grids were subsequently air-dried overnight under a Petri dish before imaging. The stained specimens were observed under various magnifications ranging from 5000× to 20,000× to assess nanoparticle distribution, and representative images were captured at 50,000× magnification (corresponding to 100 nm scale bar) using a 16 MP Matataki Flash camera (JEOL, Tokyo, Japan). The particle diameters of the final product were quantitatively measured from the TEM micrographs using ImageJ software.

2.7. Molecular docking studies

Molecular docking, a dry-lab digital technique, has increasingly become an essential tool in *in silico* drug development for predicting and evaluating molecular interactions [48]. Additionally, it is widely used to estimate drug activity, as well as to assess binding affinity and characterize intermolecular interaction patterns between different materials [49,50]. In this study, molecular docking was applied as a preliminary screening tool to evaluate the relative affinity and interaction tendencies between film-forming polymers (GEL, CH, and CMC) and the incorporated bioactive agents (AP and Eug). This computational analysis aimed to assess the strength and nature of polymer–drug interactions that may influence encapsulation efficiency, matrix stability, and subsequent drug release in locally applied formulations.

The molecular structures of AP, Eug, and CH were obtained from the PubChem database (National Center for Biotechnology Information, USA) [51]. The structure of CH was protonated to simulate acidic conditions, while GEL and CMC structures were modelled in Avogadro (Version 1.2.0) [52] using peptide and carbohydrate building blocks. All structures were geometry-optimized with the MMFF94 force field to achieve energy-minimized, stable conformations. The optimized molecules were saved in SDF format and converted to PDB files for further use. Docking simulations were performed using PyRx (Version 0.8) [53], which includes AutoDock Vina as the docking engine. GEL, CH, and

CMC were defined as macromolecules, while AP and Eug served as ligands. The docking grid box (24 × 24 × 24 Å) was centered on the polymer surface or interface region to target relevant binding sites. Multiple poses were generated for each complex, and the best conformation was selected based on the most negative binding energy (ΔG: kcal/mol). All docked complexes were visualized in BIOVIA Discovery Studio 2025 Client/ Discovery Studio Visualizer (BIOVIA, 2025 Client, Dassault Systèmes) [54] to analyze hydrogen bonds, hydrophobic interactions, and other non-covalent contacts. Interaction distances and bonding geometries were evaluated for each ligand–polymer pair. The resulting binding affinities (estimated binding free energy) are expressed in kcal.mol^{-1}, used for comparative assessment of interaction tendencies and to support hypotheses regarding possible interactions influencing formulation behavior. For each receptor–ligand pair, the best-ranked pose was selected to further calculate the dissociation constant (K_D), assuming ideal solution thermodynamics. The K_D or inhibition constant of the complex was calculated as in Eq. (2) [55].

$$K_D = e\left(\frac{\Delta G}{RT}\right) \tag{2}$$

where 'R' is the gas constant and 'T' is the absolute temperature in kelvin (310.15 K). Values were reported in millimolar units (mM).

2.8. Preparation of nanoformulation-loaded chips (dental chips)

To enhance the potential delivery of optimized NLC, which exhibited favorable characteristics such as nanoscale particle size and high EE%, NLC were further incorporated into polymeric chips. These chips were formulated using biopolymers GEL type B, CH, and CMC, selected for their biocompatibility and film-forming capabilities (Scheme 1). The chips were fabricated using a conventional solvent casting method [56–58]. Initially, GEL, CH, and CMC solutions were prepared as detailed in Table 1. CH (3% w/w) was dissolved in 1% (v/v) acetic acid, while CMC (3% w/w) and GEL (6% w/w) were separately dissolved in distilled water; all polymer solutions were prepared under continuous mechanical stirring for 90 min at elevated temperatures (50 °C for CH and 70 °C for CMC and GEL) (Scheme 1b). The resulting polymer solutions were then blended at a 1:1 ratio under continuous stirring at 40 °C. Later, glycerol was incorporated into the polymer blends at 40 wt% relative to the total polymer content. To achieve a satisfactory blend, all mixtures were heated and stirred at 40 °C for 2 h. To fabricate nanoformulation-loaded composite films, 60% (w/w) of NLC were incorporated into GEL-CH and GEL-CMC film-forming solutions, which were then stirred vigorously at room temperature for an additional 3 h to ensure uniform dispersion. The final polymer mixtures were degassed for 20 min to remove entrapped air and bubbles, followed by a 20 min rest period to ensure complete deaeration. Thereafter, 15 mL of the mixture was carefully cast onto a 60 mm glass Petri dish lined with silicone sheets. They were kept at ambient temperature until completely dried. In parallel, control films (without NLC) were prepared. Later, the films were cut into uniform chips measuring 4 mm × 5 mm. The CMC-based chips (GC40-A and GC40-B) and CH-based chips (GH40-A and GH40-B) were then wrapped in aluminum foil and stored in a desiccator until further analysis.

2.9. Technological assays

2.9.1. Chip thickness and weight uniformity measurement

Each polymeric film was cut into uniform rectangular pieces of 5 mm × 4 mm using a sharp stainless-steel cutter to ensure clean edges. The weight of each chip was determined using a digital analytical balance (LabX™ XS225 Dual range by Mettler Toledo) with a sensitivity of ±0.01 mg.

The thickness of the chip was measured using a digital micrometer (Model no. 293-821-30, Mitutoyo, Japan) to assess the uniformity and reproducibility [59] among prepared chips. For each sample, five measurements were taken at random sites, and the average thickness and SD were calculated.

2.9.2. pH determination

The surface pH of all film formulations was measured to assess their potential to irritate when applied to the oral mucosa. Each film sample was placed in a vial containing 5 mL of distilled water and allowed to swell for 5 min under ambient laboratory conditions. Following the swelling period, the pH of the solution and surface was measured by using a digital pH meter (Testo SE & Co. KGaA, Titisee-Neustadt, Germany). The electrode tip was gently placed in direct contact with the surface of the hydrated film and held in position until the reading stabilized. Measurements were performed in triplicate after 5 min, 30 min, 24 h, and 48 h, and the mean values were recorded for each film [60,61].

2.9.3. Contact angle measurement

The water contact angle was measured as part of the preformulation studies and subsequently for the optimized nanofilms. This was done to evaluate the wettability and spreading behavior of water on the surface of the film [62].

Surface wettability was assessed by measuring the contact angle of water droplets on film surfaces using a DataPhysics OCA 20 optical contact angle instrument (DataPhysics GmbH, Filderstadt, Germany). Contact angles were monitored in real-time over 40 s to assess the dynamic wetting behavior of the formulations. A 500 μL Hamilton pipette was used to dispense droplets, which were tested immediately before deposition. Measurements were recorded at 1-s intervals, using automated circle-fitting analysis *via* the SCA 20 software (DataPhysics GmbH, Filderstadt, Germany). This approach enabled precise tracking of changes in the droplet profile over time, providing detailed insights into the hydrophilic or hydrophobic nature of the prepared film surfaces [63].

2.9.4. Determination of film flexibility (% resilience)

The flexibility of the prepared films was assessed, given its impact on mechanical integrity and adaptability to the application site. The films were mounted onto a film-supporting rig (HDP/FSR), and the measurements were performed in compression test mode with Texture Analyzer (TA.XT plus, Stable Micro Systems Ltd., Surrey, UK). The experimental parameters were set to a pre-test speed of 1 mm/s, test and post-test speed of 0.5 mm/s, the trigger force of 0.5 g, and a target distance of 2 mm. After reaching the trigger force, during the test, the instrument recorded the force (mN) at the target distance and the resilience (%) of the film [64]. The obtained force–distance curve exhibited a peak when the target distance was reached.

2.9.5. Determination of burst strength/breaking force

Burst strength testing was performed to determine the films' resistance to mechanical rupture, where burst strength represents the force required to rupture the film, while the distance to burst indicates the extent of deformation before the film breaks.

Circular specimens were precisely excised from the films and mounted in a film support apparatus. Mechanical testing was performed in compression mode with the pre-test speed set at 2 mm/s, the test speed at 1 mm/s, and the post-test speed at 10 mm/s with Texture Analyzer (TA.XT plus, Stable Micro Systems Ltd., Surrey, UK). A trigger force of 1 g and a maximum target displacement of 5 mm were applied. Burst strength (mN) and distance at burst (mm) were determined from the resulting force–distance curve generated by the instrument [65].

These measurements provided insight into the mechanical robustness and elasticity of the formulated films, which are critical factors for their handling, application, and performance.

2.10. Mucoadhesive study

The mucoadhesive strength of the nanoloaded and blank films was determined using a Texture Analyzer (TA.XT plus, Stable Micro Systems Ltd., Surrey, UK) fitted with a 0.5 kg load cell. The test was performed on a modified mucoadhesion rig. A circular piece of Whatman® qualitative filter paper (Sigma-Aldrich, Budapest, Hungary) was moistened with 50 μL of mucin dispersion (8% w/w) to simulate the mucosal surface and affixed to the lower platform of the apparatus.

Each film sample was carefully attached to a 10 mm diameter cylindrical probe using a small piece of double-sided adhesive tape to ensure flat contact during measurement. The probe was then moved downward at a speed of 0.3 mm/s until the film came into full contact with the mucin-coated surface. A preload of 2500 mN was maintained for 3 min to allow intimate contact and interpenetration between the film and the mucin layer.

After the contact period, the probe was withdrawn at a speed of 2.5 mm min^{-1}. The maximum detachment force (mN) and work of adhesion (mN.mm) were recorded automatically by the Exponent Connect software (version 8.1.5.0) by Stable Micro Systems Ltd. These parameters reflect the mucoadhesive strength of the films. Each formulation was tested in quintuplicate ($n = 5$) to ensure reproducibility.

2.11. Swelling studies

The swelling properties of the dental chips loaded with NLC were measured gravimetrically. Dried chips (5 mm × 4 mm) were accurately weighed to obtain their initial dry mass, then individually immersed in 10 mL of phosphate-buffered saline (PBS, pH 7.4) maintained at 37 ± 0.5 °C with gentle shaking. At specific time intervals (5, 10, 20, 30, 60, 120, 1440, till 7200 min), each sample was withdrawn, gently blotted with filter paper to remove surface fluid, and weighed immediately to record the swelling ratio (Sr). The measurements were continued until a drop in value occurred to ensure that the chips reached their maximum level of water absorption [66]. All measurements were carried out in triplicate, and results were reported as the mean ± SD.

The swelling ratio (%) was determined using Eq. (3).

$$\text{Sr}\ (\%) = \frac{Wi - Wf}{Wi} \times 100 \tag{3}$$

where (Wi) is the initial dry weight of the chip before swelling, and (Wf) is the weight of the swollen chip.

2.12. Determination of moisture content (MC)

The solvent content in the drying films is directly proportional to their moisture content. Immediately after preparation, the films were cut to the required chip size, and moisture content measurements were carried out. To determine the moisture loss, the patches were first weighed (Mi) and placed in closed Petri dishes containing anhydrous calcium chloride within a desiccator for 5 days. The patches were removed and weighed again (Mf). The percentage of residual moisture content (MC %) was then calculated using Eq. (4) [67,68].

$$\text{MC}\ (\%) = \frac{Mi - Mf}{Mi} \times 100 \tag{4}$$

2.13. Polymer erosion (ME) study

The erosion characteristics of polymeric chips were assessed by measuring the % ME. Weighed chips were fully hydrated for a set period in saliva fluid (6.85 mM NaCl, 4.62 mM $NaH_2PO_4 \cdot 2H_2O$, 5.4 mM $CaCl_2 \cdot 2H_2O$, and 5.37 mM KCl, adjusted to pH 6.8 with a 20% sodium hydroxide solution).

The swollen chips were dried for 24 h to remove any remaining moisture. Once dried, the patches were weighed again [69]. The extent of erosion was then determined by calculating the percentage of weight loss using Eq. (5).

$$\text{ME}\ (\%) = \frac{W1 - W2}{W1} \times 100 \tag{5}$$

where (W1) represents the initial weight of the patch before wetting, and (W2) is the weight of the patch after drying, reflecting the amount of material lost due to erosion. This calculation provides a measure of the patch's erosion rate, indicating the extent of degradation or material loss during the hydration and drying process.

2.14. Raman spectroscopy and chemical mapping analysis

Raman spectroscopic analysis was performed using a DXR Dispersive Raman Spectrometer (Thermo Fisher Scientific, Waltham, MA, USA) to examine potential molecular interactions among the constituents, GEL, CH, CMC, AP, CO, and S.L in polymeric films. The spectrometer was equipped with a charge-coupled device (CCD) detector and operated with a 780 nm diode laser across the spectral region of 200–3000 cm^{-1}. Measurements were acquired using a 24 mW laser intensity and a 25 μm slit width, generating a focal area of approximately 2–3 μm. The instrument offered a spectral resolution ranging from 2.4 to 4.4 cm^{-1}. Each spectrum was obtained with an exposure duration of 6 s and averaged over 24 successive scans to improve the signal-to-noise ratio. Data acquisition and spectral processing were carried out using OMNIC™ 8.2 for Dispersive Raman software 8.3.104 package by Thermo Fisher Scientific Inc. (Waltham, MA, USA). To ensure reliable comparison among samples, spectra were normalized to minimize intensity variations.

Raman chemical imaging was used to determine the spatial distribution of NLC-A, NLC-B, AP, and CO within the film matrix. Samples were placed on aluminum foil-covered glass slides to minimize background interference and serve as supports during imaging. Raman mapping was performed using a DXR Raman Microscope (Thermo Fisher Scientific, Waltham, MA, USA) with a CCD detector for image capture. Mapping was conducted over an area of 100 × 1000 μm, with 50 μm spacing between data points, resulting in 66 spectra, each collected with a step size of 10 μm. A 780 nm diode laser operating at 12 mW and a 50 μm slit width were used throughout the mapping experiment. Individual scans were acquired after an initial 2-s laser exposure, each averaged over 32 accumulations, within the spectral range of 200–3300 cm^{-1}. Before analysis, spectra were preprocessed to correct for cosmic ray artifacts and background fluorescence. The characteristic Raman peaks of GEL, CH, CMC, NLC-A, NLC-B, AP, and CO served as spectral markers to identify and visualize their presence and distribution within the samples. Image construction and interpretation were performed using OMNIC software (Thermo Fisher Scientific, Waltham, MA, USA). For quantitative analysis of NLC distribution within the matrix, the Raman maps were processed using ImageJ [70]. Pixel intensity histograms were exported, and the coefficient of variation (CV), skewness, and kurtosis were calculated for each map to assess homogeneity, following established protocols for hyperspectral image analysis.

2.15. Drug content uniformity

Drug content uniformity was assessed by dissolving individual chips in 10 mL of a 1:1 (v/v) AcN: aqueous solvent system. Distilled water was used for CMC-based chips, whereas 1% acidified water was employed for CH-based chips to ensure complete matrix dissolution prior to analysis. The chips containing vials were vortexed using a shaker (Grant Bio™ PSU-10i Orbital Platform Shaker) until completely dissolved. Subsequently, aliquots were withdrawn and filtered through syringe filters (PVDF 0.45 μm, OlimPeak Syringe Filters by Teknokroma). The active drug concentration per chip was then quantified using a liquid chromatography technique. The total content of Eug and AP was

calculated (Section 2.16) and reported as a percentage of the loaded drugs. The % Eug and AP retention in the films was computed using Eq. (6) [71].

$$AP\ or\ Eug\ retention\ (\%) = \frac{Total\ content\ quantified\ per\ chip}{Total\ content\ loaded\ per\ chip} \times 100 \quad (6)$$

2.16. Quantification analysis

2.16.1. Eug quantification

Quantification of Eug was carried out using a SHIMADZU Nexera X2 ultra-high-performance liquid chromatography (HPLC) system (Shimadzu Corporation, Kyoto, Japan). Chromatographic separation was performed on a Phenomenex Kinetex EVO C18 reverse-phase column (250 × 4.6 mm, 5 μm particle size) with the column temperature maintained at 30 °C. The mobile phase consisted of analytical HPLC-grade water (solvent A) and methanol (solvent B), employing a gradient elution method [72]. The gradient program started with 45% solvent B, increased linearly to 75% at 7 min, and returned to 45% within the following min. The total run time was 9 min, with an injection volume of 20 μL and at a constant flow rate of 1.4 mL/min. Detection of Eug was carried out using a diode array UV–Vis detector set at 280 nm, with a retention time of approximately 6.01 min. Calibration plots exhibited linear behavior (R^2: 0.9995) generated from a 1400 μg/mL standard stock solution across the diluted tested concentrations. This method exhibited high sensitivity, with a limit of detection (LOD) of 0.63 ng/mL and a limit of quantification (LOQ) of 1.9 ng/mL.

2.16.2. AP quantification

For the quantification of AP, chromatographic analysis was conducted using a SHIMADZU Nexera X2 ultra-high-performance liquid chromatography (HPLC) system (Shimadzu Corporation, Kyoto, Japan). Separation was achieved on a Phenomenex Kinetex C18 reverse-phase column (150 × 4.6 mm, 2.5 μm) maintained at 40 °C. The mobile phase consisted of two solvents: (A) water adjusted to pH 4.5 with 85% phosphoric acid and (B) AcN. A gradient program was applied, beginning with 20% solvent B, increasing to 70% over 9 min, and then returning to the initial conditions. The flow rate was set to 0.5 mL/min, with a total analysis time of 12 min. Detection was performed using a diode array UV–VIS detector at 337 nm. The AP peak appeared at a retention time of approximately 8.4 min. The method's LOD and LOQ were determined to be 1.4 μg/mL and 4.4 μg/mL, respectively, based on a stock solution of 200 μg/mL [47].

2.17. In vitro release study

An *in vitro* release study was performed to assess the release behavior of the formulated dental chips. The NLC-loaded GC40 and GH40 chips were immersed in a release medium consisting of ethanol and PBS (1:1) and maintained under sink conditions to ensure continuous diffusion of the released compounds. The *in vitro* release study was performed using the Phoenix RDS automatic diffusion system at 37 °C with a continuous agitation speed of 200 rpm. At predetermined time intervals (0.5, 1, 2, 4, 6, 12, 18, 24, 36, 42, and 48 h, followed by every 24 h thereafter up to 7 days), 0.3 mL of the acceptor phase was automatically withdrawn and replaced with an equal volume of fresh release medium to maintain a constant release environment and sink conditions throughout the study.

For comparative analysis, both free CO (Eug) and AP-loaded chips were subjected to the same release conditions as their nano-loaded counterparts. Collected samples were analyzed (Section 2.16) to determine the cumulative release in μg from dental chips over time.

2.18. Morphological analysis of dental chip by scanning electron microscope (SEM)

The surface morphology of periodontal chips was examined by SEM before and after drug release to assess morphological changes with nanoparticle release. Both surface and fractured cross-sectional views were analyzed to evaluate erosion and structural alterations during release. Observations were performed using SEM (Hitachi S4700, Hitachi Scientific Ltd., Tokyo, Japan). The samples were coated with a gold-palladium layer using a sputter coater (Bio-Rad SC 502, VG Microtech, Uckfield, UK). The experiments were conducted with an accelerating voltage set at 10 kV and 10 mA current. The chamber pressure was kept between 1.3 and 13.0 mPa during imaging.

Quantitative morphometric analysis of SEM images was performed using ImageJ software [73,74]. Images were converted to 8-bit grayscale and thresholded to distinguish pores from the matrix. The percentage porosity was calculated as the ratio of void area to total area.

2.19. In vitro antibacterial study

2.19.1. Agar well diffusion method

The antibacterial activity was evaluated using *Aggregatibacter actinomycetemcomitans* DSM 11,122 (*A. actinomycetemcomitans*) and *Streptococcus mutans* ATCC 25175 (*S. mutans*) used as reference strains. Bacterial strains were cultured on Columbia agar supplemented with 5% sheep blood (Biomerieux, Marcy-l'Etoile, France) and incubated at 35 °C in a humidified atmosphere containing 5% CO_2 for 24 h. Bacterial suspensions were prepared by directly transferring colonies into sterile 0.85% NaCl solution, and the turbidity was adjusted to 0.5 McFarland standard (approximately 1×10^8 CFU/mL).

The standardized bacterial suspensions were evenly spread onto Columbia agar plates. Nano-loaded and blank dental chips were placed in triplicate onto the agar surface. The plates were incubated at 35 °C under 5% CO_2 conditions, and the diameters of inhibition zones (mm) were measured. Chlorhexidine digluconate-loaded chips were used as positive control, while blank films (GC40, GH40) were tested as negative controls.

2.19.2. Time kill assay

A time–kill assay was performed to evaluate the antibacterial activity of compounds released from the dental chips against *A. actinomycetemcomitans* and *S. mutans*, with modifications [75,76]. Briefly, an individual dental chip was aseptically placed into a sterile microcentrifuge tube containing 1 mL of bacterial suspension prepared in Mueller–Hinton II broth (Becton, Dickinson and Company, Sparks, MD, USA) at an initial inoculum of approximately 1×10^6 CFU/mL (colony-forming units per milliliter). The tubes were incubated at 35 °C under a humidified atmosphere supplemented with 5% CO_2. To assess the bactericidal or bacteriostatic effects of the released compounds over time, viable bacterial counts were determined at 0, 1, 3, 6, 12, and 24 h following incubation. At each time point, aliquots were collected and, when necessary, serially diluted with sterile deionized water before plating onto Columbia agar supplemented with 5% sheep blood (bioMérieux, Marcy-l'Étoile, France).

Bacterial suspensions incubated under identical conditions in the absence of a dental chip served as growth controls. All experiments were conducted in triplicate, and the data are presented as log CFU/mL.

2.20. Stability studies

Dental chips wrapped in aluminum foil were packed in an amber bottle and initially stored at temperatures of 5 ± 2 °C, 25 ± 2 °C, and 40 ± 2 °C for 6 months. After this period, samples were evaluated for physical appearance, pH, and changes in weight and thickness [77]. Based on the initial 6 months' physical parameters assessment across different thermal conditions, storage at 25 ± 2 °C was identified as optimal. Consequently, chips maintained at this temperature were assessed after an additional 3 months to quantify the % content uniformity of AP and Eug.

2.21. Statistical analysis

Data visualization and statistical evaluations were performed using GraphPad Prism version 8.0.2 (GraphPad Software, Inc., La Jolla, CA, USA). The obtained data were statistically evaluated using two-way analysis of variance (ANOVA) and subjected to Tukey's multiple comparisons test. The data are reported as the mean ± SD.

3. Results and discussions

3.1. Preliminary study

Eight mucoadhesive films (GC40-I–GH30-I) were developed by varying polymer concentration and ratios (75:25 or 50:50), with glycerol concentrations of 40% (GC40-I–GH40-I) and 30% (GC30-I–GH30-I) to the total polymer concentration, serving as a plasticizer. The concentration of glycerol in film formulations must be carefully optimized, as it significantly influences the mechanical properties and functional performance of the films. An appropriate level of plasticizer is essential to achieve a balance between tensile strength and flexibility [78].

As previously reported, increasing the concentration of glycerol raises the moisture content of hydrocolloid films due to its strong affinity for water. This is attributed to the presence of hydroxyl groups in glycerol, which interact strongly with water molecules, thus allowing the film matrix to retain water [79]. Considering the significant influence of plasticizer concentration on film properties, optimizing the plasticizer content was crucial. Based on literature guidance, glycerol was initially selected at 3 levels, 20%, 30%, and 40% (to the total weight of polymers). However, during preliminary screening, films containing 20% glycerol were brittle and mechanically weak; therefore, only the 30% and 40% concentrations were selected for physicochemical characterization.

All the films were evaluated for % resilience, surface wettability, and mucoadhesive work and force to identify the optimal film composition for oral drug delivery (Table S1).

The % resilience results confirmed the mechanical suitability of the prepared films for intra-periodontal application, ranging from 38.25% to 76.62%, indicating that both the polymer composition and the plasticizer concentration significantly affected the elastic recovery of the films. Films containing 40% glycerol exhibited noticeably higher % resilience compared to those with 30%, suggesting that the higher plasticizer level improved chain mobility and flexibility without compromising structural integrity.

Contact angle measurements ranged from 34.7° to 77.8°, indicating moderately hydrophilic surfaces that support mucoadhesion. The mucoadhesive force and work of adhesion were highest in GH30-I (863 mN) and GC30 (321 mN.mm), showing strong mucosal binding; however, these films exhibited moderate resilience and might be mechanically less stable during handling. Among all formulations, GC40 and GH40 showed the best overall balance of mechanical strength, wettability, and mucoadhesion. GC40 had the highest resilience (76.62%), an optimal contact angle (52.36°), and a strong adhesive force (664 mN), reflecting excellent elasticity and surface interaction. GH40 had a high mucoadhesive force (758 mN) and moderate resilience (60.63%), suggesting superior mucus–polymer interaction driven by CH's cationic nature and hydrogen bonding with GEL.

These properties are particularly desirable for nanoparticle-loaded periodontal films, where the formulation must remain attached under crevicular flow and mechanical stress for several days. The enhanced resilience of the 40% glycerol films allows them to resist fracture or rapid disintegration, ensuring that drug release occurs in a controlled and sustained manner over days. Previous studies have reported that films containing 40% (*w*/w) plasticizer exhibit greater homogeneity compared with those formulated with 30% (w/w) plasticizer [80]. Overall, based on the superior elasticity, adhesion strength, and surface characteristics, GC40 and GH40 with a 50:50 polymer ratio (40% glycerol concentration) were selected as the most promising and balanced formulations for prolonged residence and effective localized drug delivery in the treatment of periodontitis.

3.2. Characterization of nanoparticles

The physicochemical characteristics of the developed NLC formulations are summarized in Table 2. Both NLC-A and NLC-B exhibited nanoscale particle sizes with mean diameters of 188 nm and 160 nm, respectively, along with low dispersity indices (<0.30), indicating a narrow and homogeneous size distribution [81]. The ZP values were moderately negative (−17.2 to −17.8 mV), suggesting satisfactory colloidal stability of the formulations [82]. High EE was observed for both active pharmaceutical ingredient AP and Eug, confirming effective incorporation of the actives within the NLC matrix.

TEM is a powerful nanoscale imaging tool used to examine the morphology and surface structure at the nanoscale [83]. TEM images (Fig. 1) revealed predominantly semi-spherical to quasi-spherical nanoparticles with smooth surfaces. The particles were uniformly dispersed with minimal or no aggregation.

TEM analysis further revealed that the nanoparticles exhibited an average particle size of approximately 125 nm. The comparatively smaller particle size obtained from TEM analysis, relative to the DLS measurements, can be attributed to the fundamental differences in the measurement principles of the two techniques. Specifically, TEM determines the physical size of the nanoparticles in the dry state, whereas DLS measures the hydrodynamic diameter, which includes the solvation layer [84]. Consequently, the hydrodynamic size obtained from DLS is typically larger than the particle size measured by TEM.

3.3. Molecular docking

Molecular docking, also known as computational modeling, was performed to evaluate the intermolecular interactions between constituents of dental chips. At the atomic level, it is an important strategy for molecular binding prediction between small and macromolecules [85]. Numerous approaches based on molecular docking have been reported in the literature. For example, this method has been applied to elucidate the interaction of Eug with the critical accessory gene regulator (Agr) quorum-sensing system of *Staphylococcus aureus* and DNA, thereby enabling the identification of potential binding sites and underlying mechanisms of action [86]. In the present investigation, an analogous modeling approach was employed to systematically evaluate the intermolecular interactions between the protein (GEL), selected polymers (CH, CMC), and the bioactive compounds (AP, Eug), to provide molecular-level insight into possible interaction modes and relative compatibility among formulation components. This analysis was intended as a qualitative and comparative tool; therefore, the calculated binding energies and dissociation constants should be interpreted as relative indicators obtained under idealized conditions rather than absolute physicochemical parameters applicable to the complex polymeric system.

The docking results suggested the potential for intermolecular interactions between polymers, predominantly mediated by hydrogen bonding and hydrophobic interactions within the model. Hydrogen-bond networks were observed between GEL and CH/CMC, confirming

Table 2
NLC characterization parameters (Z_{ave}, PDI, ZP, EE of AP, and Eug).

Formulation	Z_{ave} (nm ± SD)	PDI (±SD)	ZP (mV ± SD)	EE of AP (% ± SD)	EE of Eug (% ± SD)
NLG- A	188 ± 2.5	0.25 ± 0.01	−17.2 ± 1.50	96.2 ± 1.50	94.7 ± 2.90
NLG- B	160 ± 6.2	0.23 ± 0.03	−17.8 ± 2.00	94.5 ± 1.90	94.0 ± 3.10

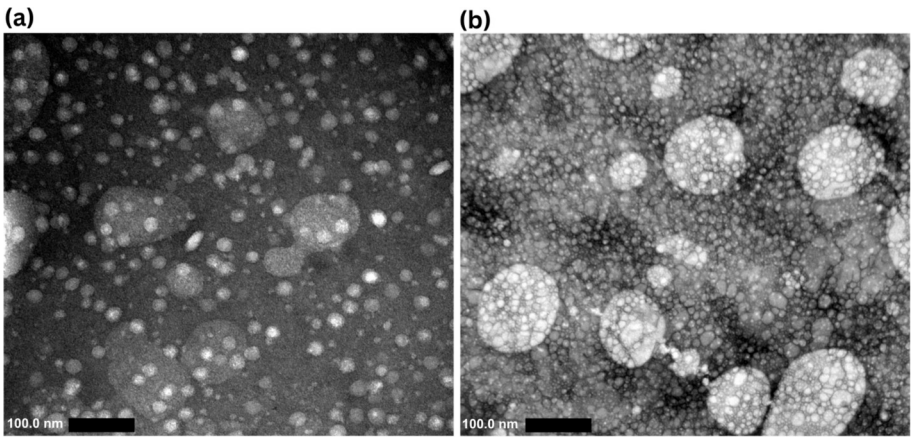

Fig. 1. Representative TEM micrographs NLC-A (a) and NLC-B (b) at magnification of 50,000× with corresponding scale bar of 100 nm.

good polymer–polymer compatibility essential for film formation. AP showed multiple hydrogen bonds and π–σ interactions with GEL, indicating favorable molecular affinity, while Eug interacted mainly *via* hydrophobic and van der Waals forces (Fig. S1). These interactions suggest effective molecular compatibility and stabilization of bioactive compounds within the GEL-based matrix, supporting their suitability for mucoadhesive drug delivery applications. Similarly, previous molecular docking studies have identified hydrogen bonds, π-alkyl, π-π, and van der Waals interactions as the primary forces mediating phytochemical (curcumin)–GEL complexation [87].

To provide a comparative, semi-quantitative ranking of interaction strengths, binding affinities, and corresponding dissociation constants were calculated (Fig. 2). All complexes exhibited negative ΔG values, indicating energetically favorable interactions within the docking model, while lower calculated K_D values suggest stronger relative binding within the docking framework. Among the biopolymeric combinations, GEL–CH showed comparatively higher ΔG and lower K_D values, suggesting potential compatibility that can facilitate the development of robust, well-integrated films. The GEL–AP and CH–AP complexes displayed the increased binding affinity, evidenced by a more negative ΔG and the lowest K_D, suggesting a favorable interaction with GEL at the molecular level, through hydrogen bonding and π–π interactions. In contrast, GEL–Eug exhibited moderately higher K_D values, reflecting weaker yet favorable binding dominated by hydrophobic interactions. This *in silico* prediction correlates strongly with our experimental observations, as CH-based chips exhibited sustained drug release and superior matrix stability, whereas CMC-based chips displayed

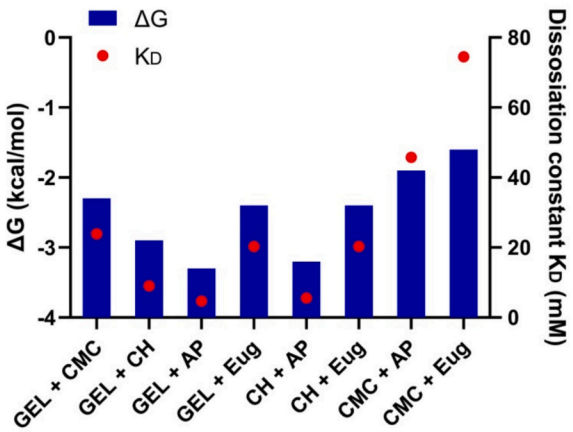

Fig. 2. Relative thermodynamic (ΔG) and dissociation index (K_D) from *in silico* docking, shown as model-dependent qualitative ranking to correlate with experimental observations.

comparatively accelerated release behavior and rapid matrix erosion. Molecular docking analysis was previously performed by Bhatia et al. to evaluate the interaction and complexation behavior between the drug and hydrocolloid polymers. Their study demonstrated that polymers such as GEL, CMC, and sodium alginate can form intermolecular complexes capable of accommodating the drug within the polymeric network, as indicated by highly negative docking scores [88].

Altogether, the qualitative interaction profiles and relative binding rankings from docking analysis provide a useful, hypothesis-generating tool to rationalize the experimental observations of polymer compatibility, drug release, and matrix performance.

3.4. Characterization of nanoparticles loaded dental chips

The fabricated periodontal chips exhibited good uniformity in both weight and thickness throughout the matrix system. The mean weight ranged from 14.38 ± 0.28 mg to 14.61 ± 0.24 mg, indicating minimal batch-to-batch variation. Similarly, the thickness of the chips was consistently maintained between 0.34 ± 0.02 mm and 0.36 ± 0.01 mm. No statistically relevant differences were observed among the formulations, suggesting that the composition did not adversely affect the dimensional consistency of the chips. The uniform thickness and weight are desirable attributes for periodontal application, ensuring reproducible drug loading and ease of insertion into periodontal pockets.

The solution and surface pH of the periodontal chips were evaluated to assess their potential to irritate the oral mucosa and gingival tissues. Surface and solution pH values were measured after 5 min (Table 3) and were subsequently monitored at 24 and 48 h. Over time, only minimal variations were observed between the surface and solution pH values. After 48 h, the pH remained relatively stable, indicating good pH compatibility.

The oral cavity normally maintains a near-neutral pH of 6.7–7.3. Microbial carbohydrate metabolism produces acids, causing a lowering of the pH, while urea and sialin breakdown generate ammonia and raise the pH. Limited salivary diffusion in plaque allows acid accumulation, and post-sugar intake (plaque pH) can drop below 5.0, promoting aciduric bacteria and dental caries [89]. Moreover, inflammation creates a mildly acidic microenvironment (pH 5.0–7.0), which promotes the growth of pathogens such as *Prevotella intermedia* and *Fusobacterium nucleatum* [90]. Hence, the pH of the formulated periodontal chips is compatible with the oral environment, minimizing irritation while enabling targeted drug delivery, and falls within the acceptable range for mucosal tolerance (pH 5.6–7.4), as reported by another research group [91].

The mechanical resilience of the films was also evaluated post-encapsulation to assess the influence of NLC loading on the elastic recovery of the polymeric network. Both types of formulations maintained

Table 3
Physical properties of dental chips loaded with nanocarriers.

Formulations	Weight uniformity (mg ± SD)	Thickness (mm ± SD)	Surface pH (±SD)	Solution pH (±SD)	Resilience (% ± SD)	Burst force (mN ± SD)
GC40-A	14.38 ± 0.28	0.35 ± 0.02	6.93 ± 0.02	7.01 ± 0.01	68.37 ± 0.21	2696.6 ± 29.10
GC40-B	14.47 ± 0.20	0.36 ± 0.03	6.83 ± 0.03	7.00 ± 0.02	67.71 ± 0.15	3736.3 ± 16.17
GH40-A	14.58 ± 0.27	0.34 ± 0.02	5.65 ± 0.02	6.60 ± 0.11	60.25 ± 0.23	2450.5 ± 23.02
GH40-B	14.61 ± 0.24	0.36 ± 0.01	5.70 ± 0.01	6.75 ± 0.13	62.30 ± 0.18	3291.0 ± 38.90

acceptable resilience values, confirming that the integration of the lipid phase slightly changes the structural flexibility of the films.

Lipid incorporation is known to influence the structural continuity and mechanical behavior of protein-based films. Generally, pure protein films exhibit higher tensile strength and flexibility than composite films containing lipids, as the presence of lipids may disrupt the continuous polymer network [92].

Several studies have reported a reduction in tensile strength with increasing lipid concentration in films prepared from materials such as GEL, gellan, sodium caseinate, wheat gluten, and whey protein isolate. This effect is commonly attributed to the partial replacement of polymer chains by lipid molecules within the matrix. Moreover, the extent of this effect depends on the characteristics of the lipid and its ability to interact with the protein network [93–95].

In the present study, the incorporation of nano lipidcarriers into the biopolymer films resulted in a slight reduction in resilience, which may be associated with the partial disruption of the polymer network due to lipid incorporation. The CMC-based blank films demonstrated a resilience of 76.62% that slightly decreased to 68.37% after lipid nanocarriers loading, whereas the CH-based blank film (60.63%) showed a slight difference in value as the loaded films (62.30%) (Table 3). This difference between the two types of formulations can also be attributed to the molecular mobility imparted by the matrix, which promotes elastic behavior and facilitates structural recovery following deformation. The marginally lower resilience in CH is consistent with the more rigid and cationic nature of CH, whose intermolecular hydrogen bonding provides structural strength at the expense of flexibility. Molecular modeling suggested the same behavioral pattern, where the binding affinity is higher between GEL–CH as compared to GEL–CMC.

Collectively, both systems exhibited mechanical robustness suitable for mucosal application, with the CMC compositions showing marginally superior elastic recovery, an advantageous property for maintaining film integrity during application and prolonged adhesion at the target site.

Mechanical strength was further assessed through burst force measurements, performed only on the NLC-loaded films, as the blank formulations exceeded the upper limit (5 kg load cell) of the testing instrument. This limitation itself reflected the high tensile robustness of the unmodified films. Post-encapsulation, the burst strength values remained within the desirable range for flexible yet durable mucoadhesive matrices. The CMC-based films exhibited higher burst force values, compared to their CH-based counterparts, showing 2696 mN and 3736 mN (Table 3). This consistent enhancement suggested the improved matrix densification and possible intermolecular interactions between the lipid components and the polymeric network, which reinforce structural cohesion.

Taken together, both CMC- and CH-based films maintained adequate mechanical integrity, which is a critical factor for ensuring physical durability during handling, application, and retention in the mucosal environment.

3.5. Contact angle

Contact angle assessment provides useful data on the wettability characteristics of the film surface [96]. After NLC loading, a slight increase in contact angle was observed in CH-based films, indicating minor surface modification and possible migration of lipid components to the air–film interface. CMC-based films, the contact angle remained almost the same (unloaded: 52.36°; loaded: 53.70° and 52.88°), while the CH-based formulations showed an upward trend, rising from 54.19° to 61.79° and 59.65°. This modest increase suggests that NLC encapsulation slightly reduced hydrophilicity. The presence of lipids in the NLC, owing to their non-polar nature, contributed to increased film hydrophobicity and enhanced surface lipophilicity. This phenomenon is well-documented in the literature, where a similar trend of increase in hydrophobicity is observed after lipid incorporation in CH films [97] and basil seed gum films [98].

Nevertheless, the films retained sufficient wettability to maintain mucoadhesive potential, confirming that NLC incorporation did not compromise surface compatibility with biological tissues. These findings validate the structural stability of the optimized film matrices following NLC loading, providing a promising platform for controlled release of actives within mucosal environments.

3.6. Mucoadhesive study

Mucoadhesion involves polymer hydration, chain interpenetration with mucin, and stabilization through intermolecular forces, including hydrogen bonding, electrostatic, hydrophobic, and van der Waals interactions [99]. CH, a well-known mucoadhesive polymer, exhibits strong mucoadhesion primarily due to electrostatic interactions between its positively charged groups and the negatively charged mucin [100]. Additionally, increasing the concentration of the polymer can influence these interactions, enhancing mucoadhesion by promoting greater physical entanglement between the polymer and the mucosal surface. A fundamental mechanism of mucoadhesion consists of two key steps: (i) the establishment of close contact between the bioadhesive and the membrane, which may involve wetting or swelling, and (ii) the infiltration of the bioadhesive into the tissue or the surface of the mucus membrane through interpenetration [101].

The incorporation of NLC into the optimized film matrices resulted in notable changes in mucoadhesive characteristics. Both formulations retained strong adhesion to mucosal substrates, indicating that NLC integration did not impair the films' surface interactions with mucin.

In the CMC-based chip series, the mucoadhesive force increased markedly from 664 mN (blank chip) to 1206 mN for the NLC-loaded chip (Fig. 3a), while the work of adhesion exhibited a relatively modest rise, from 128 mN·mm to 167 mN·mm upon NLC incorporation (Fig. 3b). This pattern suggests a denser film–mucus interaction, possibly due to improved interfacial contact facilitated by lipid-mediated flexibility. Improved resilience and swelling behavior of CMC chips also affirm the improved mucoadhesive results. Similarly, the CH-based films exhibited a rise in adhesive force from 758 mN up to 965 mN and an increase in work of adhesion from 102 to 125 mN·mm with nanoparticle loading, implying enhanced electrostatic and hydrogen-bonding interactions between protonated amino groups of CH and mucin glycoproteins.

Overall, NLC incorporation improved mucoadhesive performance, particularly in the CMC-based system, indicating that the lipid–polymer hybrid network effectively maintained bioadhesive properties while promoting prolonged residence at the site of application.

3.7. Moisture content and polymer erosion

The moisture content of orally administered dental chips plays a

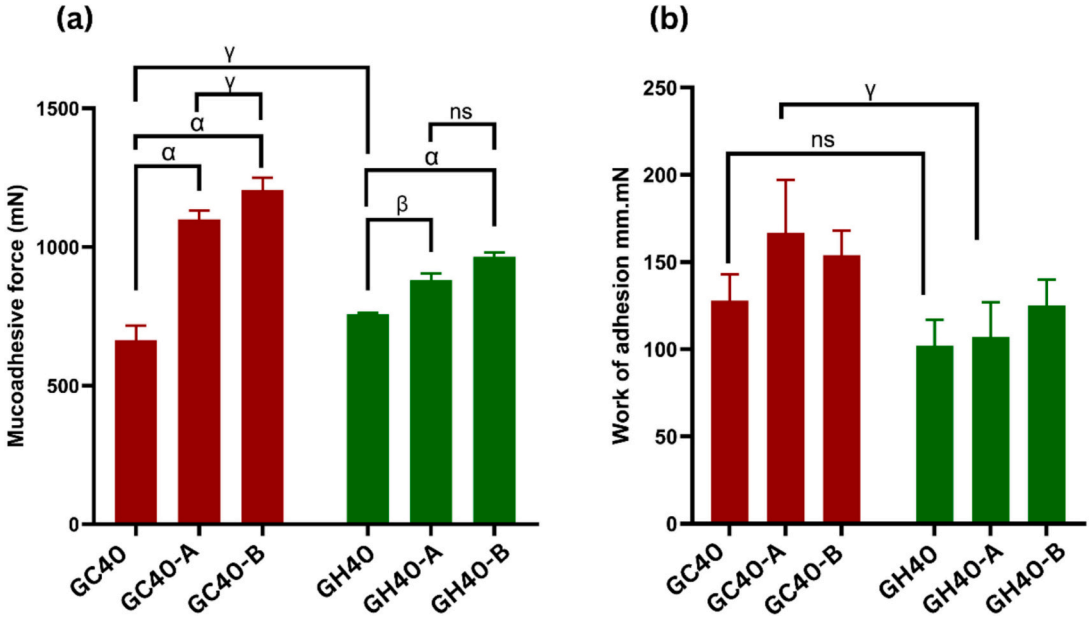

Fig. 3. Comparison of mucoadhesive force (a) and work of adhesion (b) of nanoloaded and blank chips, presented as means ± SD. Statistical significance between both types of loaded and blank formulations was determined using two-way ANOVA followed by Tukey's multiple comparison test. Symbols denote levels of significance as follows: γ indicates $p < 0.05$; β indicates $p < 0.01$; α indicates $p < 0.0001$; and "ns" denotes non-significant differences ($p > 0.05$).

critical role in determining their brittleness and friability. An appropriate balance among formulation components regulates the residual moisture content, which directly influences both the mechanical integrity and functional performance of the chips. Consequently, the evaluation of hydrophilic and hydrophobic polymeric chips typically includes measurements of water absorption capacity and polymer erosion to comprehensively assess their performance. According to the literature, an ideal buccal film formulation should exhibit a moisture content below 5% [102], as higher values may compromise film stability and handling properties. The moisture content of the formulated chips was low and consistent across all samples, with mean values ranging from 1.81% to 1.90%. The associated SDs (0.24–0.50%) indicate acceptable uniformity among formulations. All samples exhibited moisture levels well below the documented threshold of 5% for buccal films, suggesting adequate stability and reduced risk of brittleness or friability (Fig. 4).

Among the evaluated chip formulations, the GC40 matrices exhibited higher mean matrix erosion compared to the CH-based counterparts. Specifically, the GC40-A batch demonstrated the erosion extent at 45.2 ± 2.04%, while GC40-B showed a slightly lower but comparably elevated erosion of 44.82 ± 3.38%.

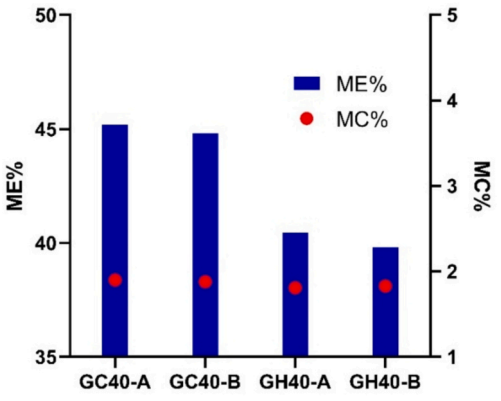

Fig. 4. Comparative analysis of matrix erosion and moisture uptake for GEL–CMC (GC40) and GEL–CH (GH40) chip formulations. The bar graph represents mean matrix erosion (ME%) for GC40-A, GC40-B, GH40-A, and GH40-B. Superimposed circle markers denote corresponding mean moisture content (MC %) values for each formulation.

In contrast, the GEL–CH matrices displayed reduced erosion, with GH40-A and GH40-B presenting mean values of 40.45 ± 0.01% and 39.80 ± 1.37%, respectively. The near-identical erosion values for the GH40 series indicate a consistent erosion profile. Overall, the data indicate that incorporating CH into the GEL network confers a modest reduction in matrix erosion compared with GEL–CMC chips. These differences in erosion behavior reflect formulation-dependent differences in matrix stability, which are critical for tailoring material performance in applications requiring controlled degradation kinetics.

When polymeric materials come into contact with mucosa, several sequential processes occur, including penetration of water molecules into the polymer network, hydration, swelling, polymer chain relaxation, and eventual erosion. Water diffusion into the matrix forms a thin gel-like layer on the film surface. As the matrix becomes hydrated, the incorporated drug begins to diffuse outward. Greater penetration of the aqueous medium into the polymer matrix results in increased drug release [102], this is in agreement with our release profile, where CMC-based chips exhibited superior drug release compared to CH-based formulations.

3.8. Swelling index

Swelling ability is a key property of oral chips for two main reasons. First, water absorption enhances the bioadhesive interaction between the dental chip and the mucosal surface, which largely depends on the characteristics of the polymer matrix. Second, hydration of the chip facilitates drug release, mainly through diffusion, polymer relaxation, swelling, and erosion mechanisms. A direct correlation between the extent of water absorption and drug dissolution has already been reported in the literature [103].

The swelling ratio of the NLC-loaded chips was evaluated over a prolonged period (0–7200 min) to assess the hydration capacity and structural stability of the polymeric matrices. All chips exhibited a characteristic biphasic swelling profile, characterized by an initial rapid uptake of fluid during the first hour, followed by a slower equilibrium phase that extended throughout the observation period.

The CMC-based chips (GC40-A and GC40-B) demonstrated greater water uptake compared with the CH-based systems. Within the first 45 min, the swelling ratio increased sharply from zero to approximately 95%, reaching a near-equilibrium state by 165 min (≈105–111%). The highest level of swelling (117%) achieved in 720 min that decresed to 110% in the next 720 min (Fig. 5). The high hydrophilicity of CMC and its ability to form an open gel network promoted efficient fluid penetration and chain relaxation. These findings were further supported by SEM micrographs, which revealed morphological features consistent with enhanced swelling behavior.

By contrast, the CH-based chips (GH40-A and GH40-B) exhibited slower and more controlled hydration. The swelling ratio increased steadily from 20 to 27% at 5 min to around 65% after 48 h, reaching a maximum of approximately 72% at 96 h (5760 min). Beyond this point, a slight reduction to below 70% was observed over the next 24 h. This moderated swelling behavior reflects the denser polymeric network and stronger intermolecular hydrogen bonding of CH, which restricts water diffusion.

The swelling characteristics of the chips are strongly influenced by their structural properties and formulation composition. As expected, chips incorporating hydrophobic polymers exhibited lower hydration levels compared with those composed of hydrophilic materials, a trend that is clearly reflected in our results.

Overall, both types maintained structural integrity throughout the swelling test, with CMC-based systems showing faster hydration and higher equilibrium swelling, while CH-based systems demonstrated slower, more sustained water uptake. These contrasting profiles are advantageous for tailoring chip performance as CMC matrices may facilitate quicker mucoadhesive hydration and drug diffusion, whereas CH chips provide greater dimensional stability for prolonged mucosal residence and drug release.

3.9. Raman interaction and mapping

The Raman spectra of the pure components and composite films (Fig. 6) show characteristic vibrational modes, confirming the incorporation of AP and CO into the polymer matrices.

Consistent with other flavone derivatives, AP displays its most intense Raman band near 1600 cm^{-1}, primarily associated with the C═O stretching vibration coupled with $C_2 = C_3$ or quinoid-type ring stretching. Additional features between 1400 and 1500 cm^{-1} arise from in-plane bending of hydroxyl groups. A distinct and sharp band around 1245 cm^{-1} corresponds to the combined contribution of 7-OH bending and C—H bending modes. The ring B trigonal stretching vibration, which is typically more prominent in other flavones and commonly

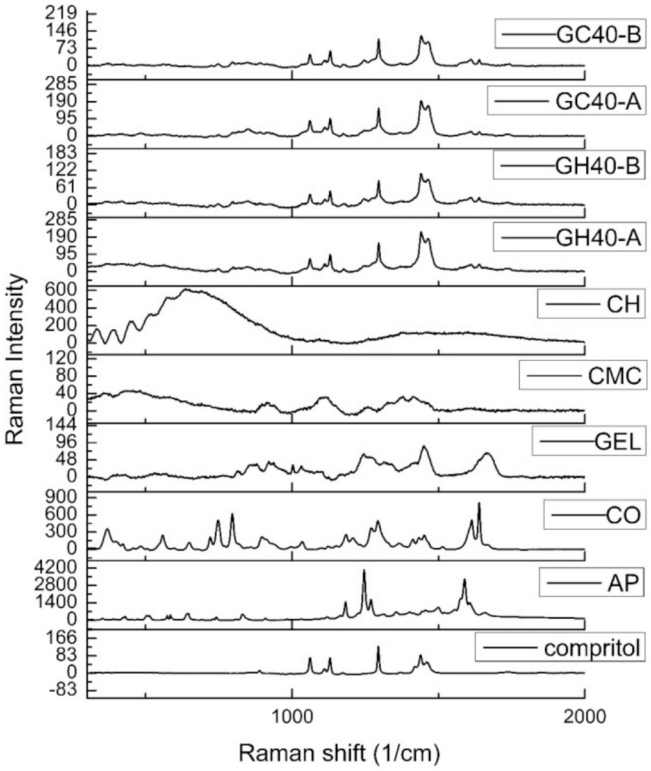

Fig. 6. Raman spectra of individual components, including S.L (Compritol), AP, CO, GEL, CMC, and CH, are presented along with formulated samples (GC40-A, GC40-B, GH40-A, and GH40-B). S.L exhibits characteristic lipid bands mainly associated with C—C stretching and CH deformation vibrations in the region of ~1060–1130 cm^{-1} and ~1290–1450 cm^{-1}. AP and CO show distinct sharp peaks corresponding to their crystalline structures, while GEL, CMC, and CH display broader bands typical of polymeric and amorphous materials. The Raman spectra of GC40 and GH40 formulations (both A and B) show the presence of characteristic peaks of the constituent components without the appearance of new bands or significant peak shifts, indicating the absence of chemical interactions and confirming good compatibility between the active component and excipients within the formulations.

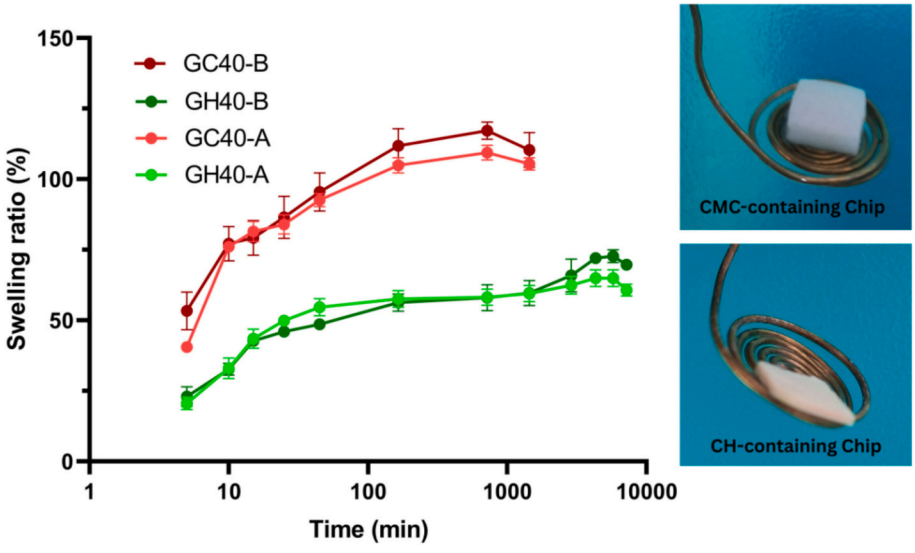

Fig. 5. Time-dependent swelling ratio profiles of CMC-based and CH-based NLC-loaded dental chips.

appears near 1000 cm^{-1}, is shifted to approximately 983 cm^{-1} in AP and exhibits only weak intensity. These characteristic vibrational features collectively define the spectral fingerprint of AP, facilitating its identification within the composite film matrix [104,105].

The CO spectrum showed peaks at approximately 1273 cm^{-1} attributed to Ar—O stretching, and another at 1036 cm^{-1} corresponding to C—O stretching of Eug. The molecular structure of Eug features a carbon-carbon double bond, corresponding to a characteristic absorption band observed between 1680 and 1600 cm^{-1}, attributed to C=C stretching vibrations. Moreover, a band observed around 900 cm^{-1} is characteristic of the wagging motion of the monoalkyl ethylene group (R–CH=CH_2), and a band at 801 cm^{-1} is assigned to C—O stretching of benzyl alcohol [106,107].

In nanoparticles loaded GEL–CMC and GEL–CH chips, the characteristic peaks of AP and CO remained detectable, albeit with reduced intensity and slight shifts toward lower wavenumbers. This attenuation and slight band displacement indicate strong intermolecular interactions, likely hydrogen bonding between the polymeric matrix and the functional groups of AP and Eug, as well as possible confinement effects of the lipid carriers. The retention of the major characteristic peaks confirms that both bioactives remain chemically stable within the nano-dental chips, while the spectral shifts substantiate their successful molecular entrapment and compatibility with the GEL-based systems.

The Raman mapping profiles of the hybrid GEL–CMC and GEL–CH matrices revealed distinct spatial distribution patterns of the incorporated NLC components. In both systems, the characteristic peaks of AP and CO were clearly detected, confirming their successful entrapment within the polymeric chips. The GEL–CH matrix exhibited sharper and more homogeneous signal distribution, suggesting stronger intermolecular interactions and better compatibility between CH and the lipid–polyphenolic constituents (Figs. 9, 10). While the GC40-A chip (Fig. 7) presented a well-distributed arrangement of nanoparticles, the GC40-B chip (Fig. 8) yielded a slightly less homogeneous dispersion of NLCs. Overall, the mapping data demonstrate that both polymeric systems effectively embed AP and CO, with the CH-based formulation showing a more compact molecular organization and superior component retention.

Quantitative analysis of chemical mapping, based on mean intensities, CV, and morphometric histogram parameters (skewness and kurtosis), provides critical insight into the physical dispersion state of NLC within the respective biopolymeric networks (Fig. S2 and Table S2). Skewness measures the degree of asymmetry relative to the mean [108], indicating how a distribution deviates from the symmetry of a normal distribution [109]. Kurtosis describes the peakedness or flatness relative to the normal distribution [110]. In the CH-based series, positive kurtosis values (0.207 and 1.590) indicate a highly peaked, leptokurtic distribution. In contrast, the CMC-based series exhibited negative kurtosis (−0.177 and −0.194), reflecting a platykurtic (flatter) distribution within the system [111]. According to the literature, skewness and kurtosis values within the range of −2 to +2 are considered acceptable for assuming a normal univariate distribution [112,113]. Although all the formulations exhibited values within this acceptable range, the CH-based chips demonstrated superior performance due to their lower variance and positive kurtosis, reflecting a well-dispersed NLC within the system.

3.10. Content uniformity

The content uniformity of the prepared dental chips was evaluated for both Eug and AP. All formulations demonstrated consistent drug loading, with percent content values ranging from 95.5% to 97.6% (Table 4). This indicates that the drugs were uniformly distributed within the chips, confirming the reliability and reproducibility of the chip preparation method.

3.11. Release study

The release of drugs from NLC and matrix systems is governed by multiple factors, including the drug's lipophilicity, the composition and concentration of the NLC components, and the structural characteristics of the polymeric materials [114].

The *in-vitro* release study revealed distinct release behaviors for CMC- and CH-based chips loaded with either free Eug or Eug-encapsulated nanoparticles under simulated physiological conditions (37 °C with continuous agitation). All formulations exhibited an initial burst release during the early time points, attributable to the rapid diffusion of surface-associated Eug; however, the magnitude of this burst was markedly higher for CMC chips, particularly those containing free Eug. Nanoparticle-loaded CMC formulations showed a relatively moderated release compared to free Eug CMC-based chips (GC-free-Eug), indicating that nanoencapsulation prolongs the drug release, as previously reported in the literature [115]. Nevertheless, the cumulative release from CMC systems increased rapidly within the first 24–48 h, reaching values exceeding ~1200 μg, after which the study was discontinued due to a partial loss of chip integrity. The comparatively rapid disintegration of CMC chips is most plausibly attributed to the highly hydrophilic nature of CMC, which undergoes excessive swelling and erosion under constant stirring and elevated temperature, leading to matrix scattering.

In contrast, CH-based chips demonstrated superior structural

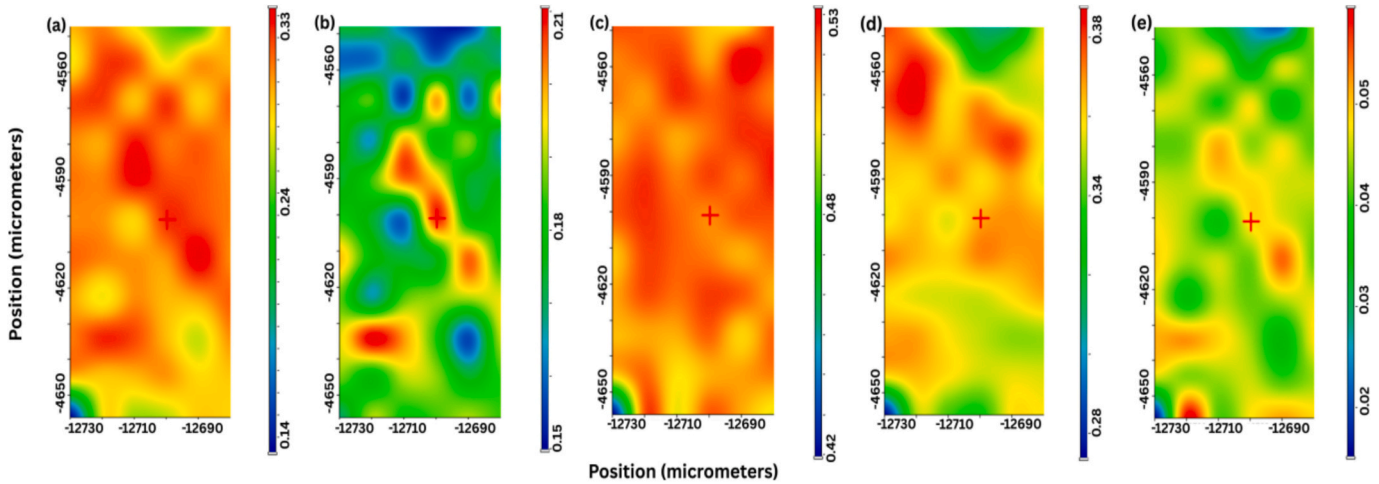

Fig. 7. Raman Mapping GC40-A of dental chip: GEL (a), CMC (b), NLC-A (c), CO (d), AP (e).

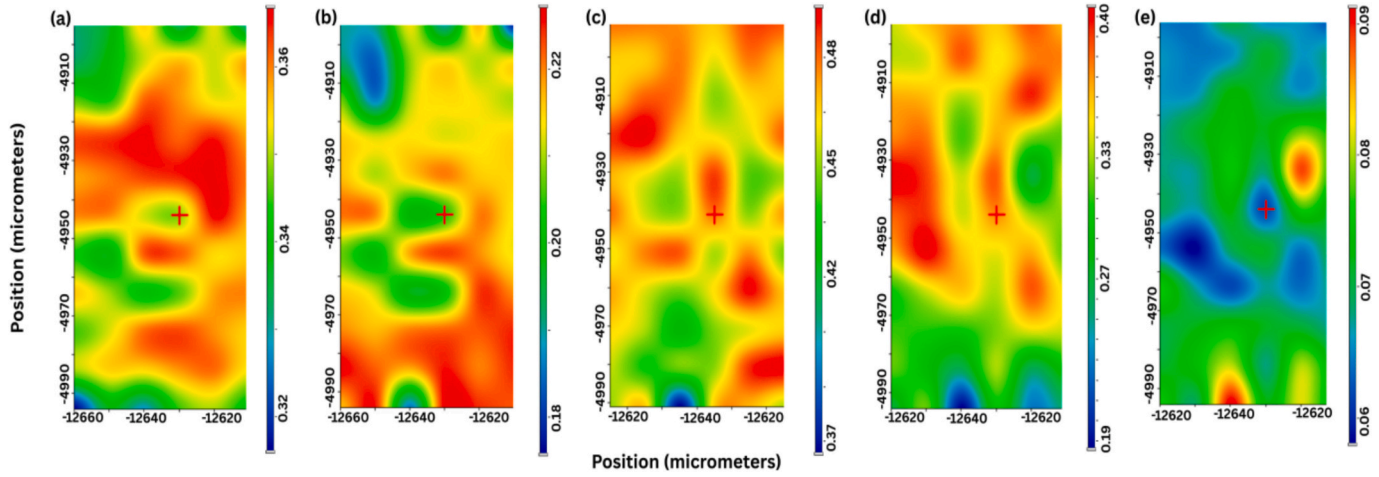

Fig. 8. Raman Mapping of GC40-B dental chip: GEL (a), CMC (b), NLC-B (c), CO (d), AP (e).

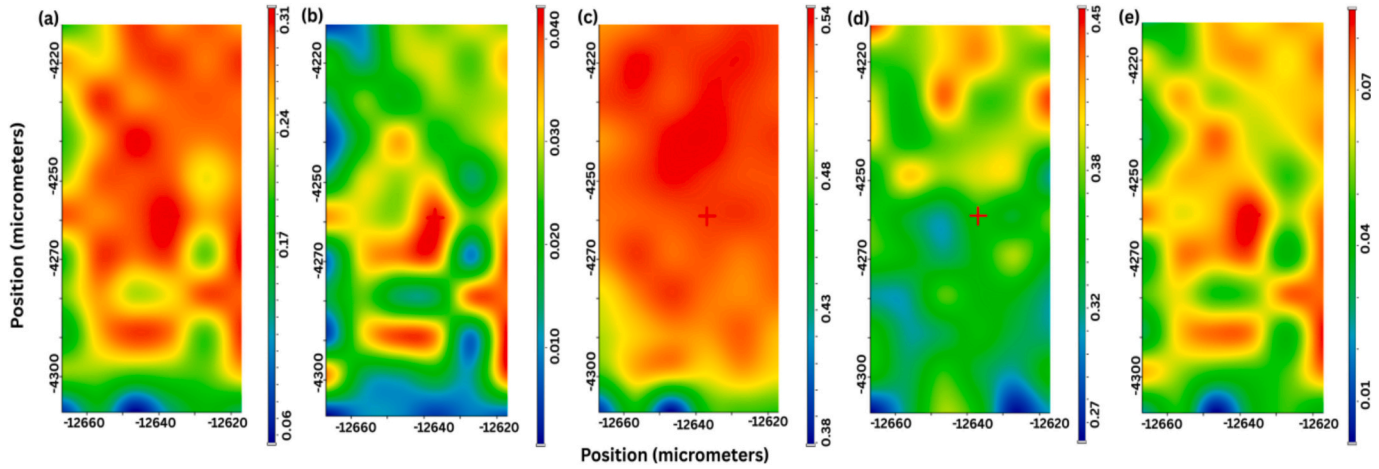

Fig. 9. Raman Mapping of GH40-A dental chip: GEL (a), CH (b), NLC-A (c), CO (d), AP (e).

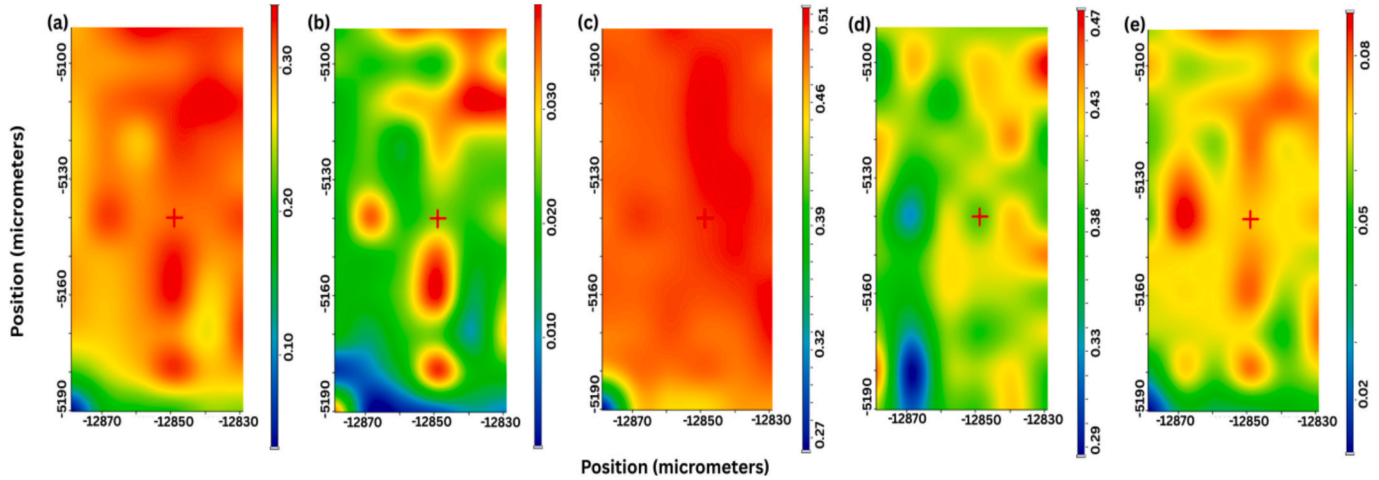

Fig. 10. Raman Mapping of GH40-B dental chip: GEL (a), CH (b), NLC-B (c), CO (d), AP (e).

stability and more sustained release profile. Although an initial burst was observed, the release rate gradually stabilized, reflecting controlled diffusion of Eug from the polymeric matrix. Nanoparticle-loaded CH chips consistently exhibited more regulated release compared to CH chips containing free Eug, highlighting the role of nanoparticles as secondary drug reservoirs that delay diffusion and enhance retention within the matrix (Fig. 11a). The comparatively slower hydration, stronger polymer–drug interactions, and semi-crystalline nature of CH contributed to reduced erosion and prolonged release kinetics. This analysis indicates that CMC chips promote relatively rapid drug release,

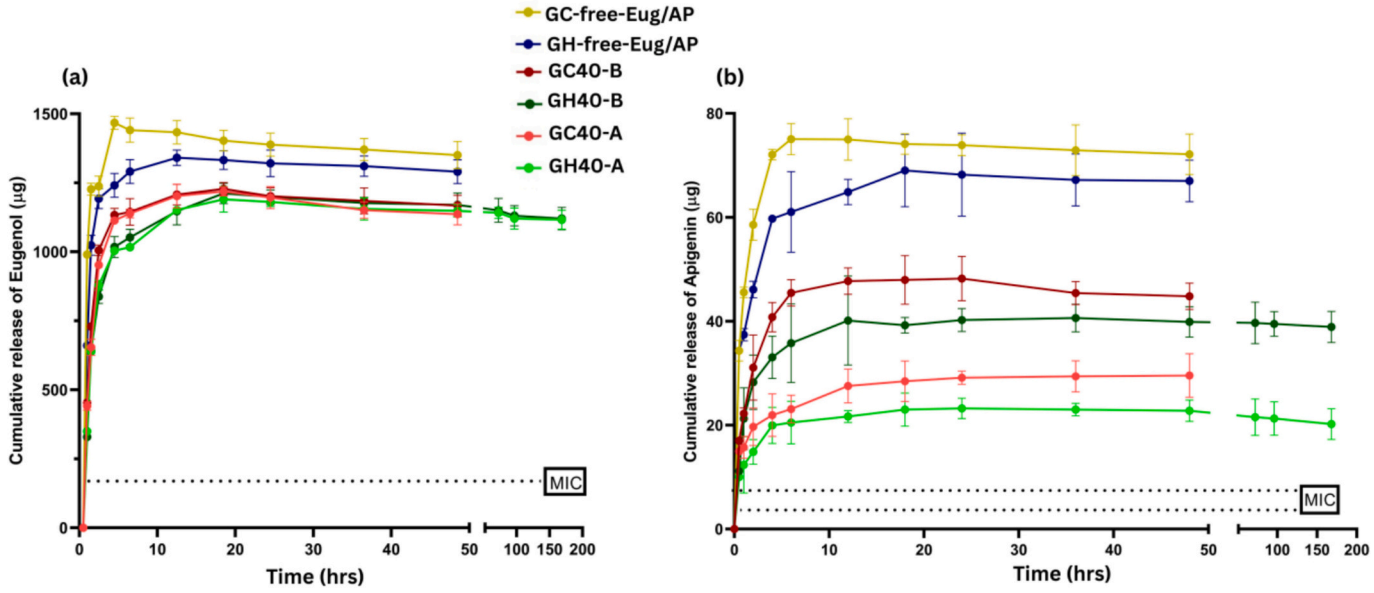

Fig. 11. *In vitro* release profile of Eug (a) and AP (b) from CMC- and CH-based dental chips.

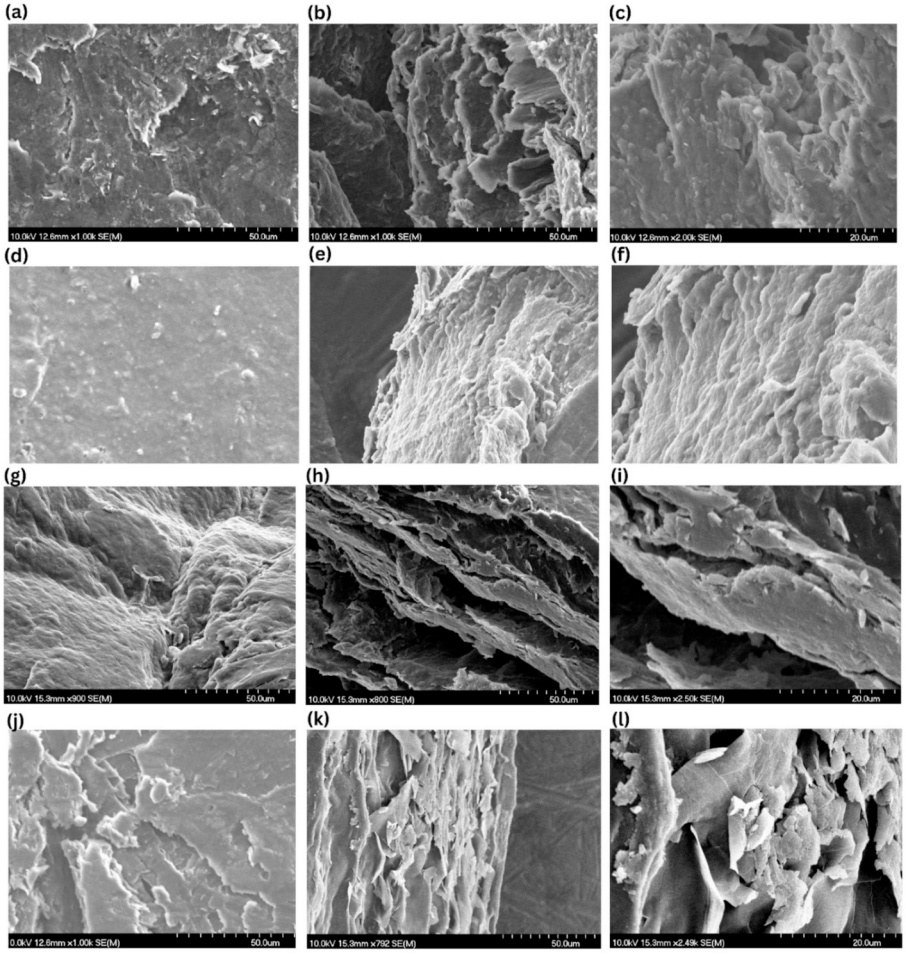

Fig. 12. SEM morphological analysis of optimized CMC-based nano-dental chips before release: surface of chip (a), cross-section at 50 µm, and at 20 µm (b,c): CH-based nano-dental chip before release: surface of chip (d), cross-section at 50 µm, and at 20 µm (e,f): CMC based nano-dental chip after release: surface of chip (g), cross-section at 50 µm, and at 20 µm (h,i): CH-based nano-dental chip after release: surface of chip (j), cross-section at 50 µm, and at 20 µm (k,l).

whereas CH-based nanoparticle-loaded chips enable more sustained Eug delivery. All formulations exhibited an initial burst release during the early hours, which is commonly associated with the rapid diffusion of surface-associated Eug.

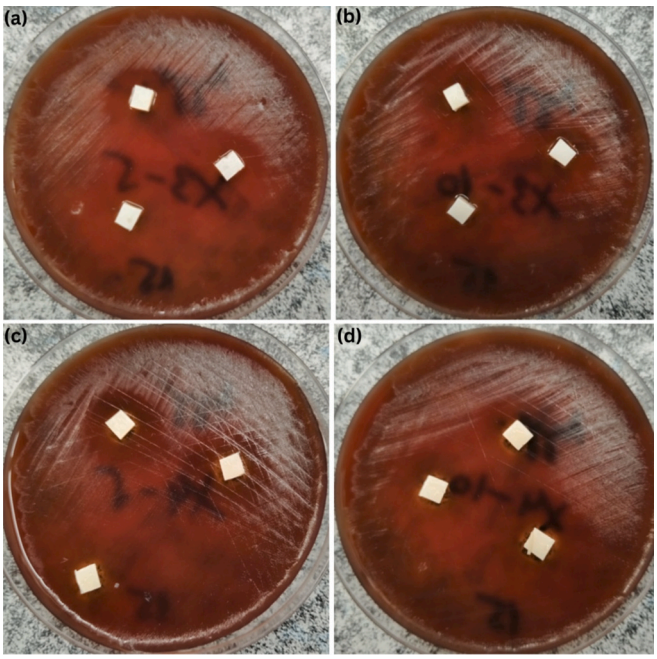

Fig. 13. Antibacterial activity against *A. actinomycetemcomitans* expressed as zones of inhibition for GC40-A (a), GC40-B (b), GH40-A (c), and GH40-B (d).

The *in-vitro* release profile of AP from CMC- and CH-based chips demonstrated a formulation and polymer-dependent release behavior under physiological conditions (Fig. 11b). All formulations showed an initial burst release within the first 0.5–2 h, which can be attributed to the rapid diffusion of free or nanoloaded AP loosely associated with the chip surface. Among the CMC-based nanoparticle-loaded chips, AP release increased rapidly during the early time points, reaching approximately 27–47 μg within 6–12 h, with GC40-B consistently exhibiting higher cumulative release than GC40-A due to the increased drug loading. Chips containing free AP in CMC (GC-free-AP) showed an even more pronounced initial release, confirming the absence of diffusional barriers typically provided by nanoparticle encapsulation. However, similar to the Eug study, CMC-based chips lost their structural integrity beyond 48 h as a result of excessive swelling and erosion caused by constant stirring and incubation at 37 °C, leading to chip scattering and necessitating the termination of the release study.

CH-based chips showed superior matrix stability and sustained AP release, with the initial burst gradually stabilizing. Nanoparticles further prolonged and regulated AP release, acting as secondary reservoirs. Conclusively, the release profile can be explained by two mechanisms: an initial rapid release of active moieties localized on or adsorbed to the film surface, and a subsequent sustained release governed by diffusion and/or erosional processes within the film matrix [116]. When considered together, *in vitro* release studies showed that nanoparticle-loaded formulations outperformed free-drug-loaded chips, demonstrating that nanoparticle entrapment and stronger polymer–drug interactions collectively prolonged drug diffusion.

3.12. Morphological analysis of dental chips

The surface morphology of the prepared dental chips containing nanoparticles was examined by SEM, micrographs are presented in Fig. 12. The nanoparticle-loaded chips displayed a slightly rough and heterogeneous surface texture, indicating that the incorporation of nanoparticles may have altered the surface topography of the matrix [117]. This trend aligns with earlier reports on NLC-loaded buccal films fabricated with hydroxypropyl methylcellulose, possessing rough surface morphology and a loosely organized internal structure [116]. Furthermore, the evaporation-driven casting process likely facilitated matrix consolidation, leading to the development of nodular domains within the structure, a feature commonly associated with solvent-cast biopolymer films [118]. However, no visible aggregation or large clusters of nanoparticles were observed in the composite chips. The absence of noticeable agglomeration indicates good compatibility between the nanoparticles and the polymer network, which may contribute to the structural integrity and controlled drug release behavior from the chips.

Post-release SEM analysis revealed distinct morphological differences between GEL–CMC and GEL–CH chips, closely correlating with their respective drug release behaviors. The CMC-based chips (Fig. 12(g, h,i)) exhibited pronounced swelling, delamination, and matrix fragmentation. The surface and cross-sectional images showed the formation of irregular-shaped gaps and pores, attributed to the leaching of the water-soluble polymer during dissolution [119]. Additionally, the presence of fissures and collapsed lamellar structures indicates that drug release occurred primarily through swelling-induced diffusion

Table 4
Content uniformity of active constituents in dental chips, expressed as percent drug content (%).

Dental chips	Eug content (% ± SD)	AP content (% ± SD)
GC40-A	95.5 ± 2.1	95.8 ± 1.5
GC40-B	96.8 ± 1.5	96.6 ± 1.4
GH40-A	96.1 ± 2.3	97.0 ± 0.9
GH40-B	97.5 ± 1.8	97.6 ± 1.0

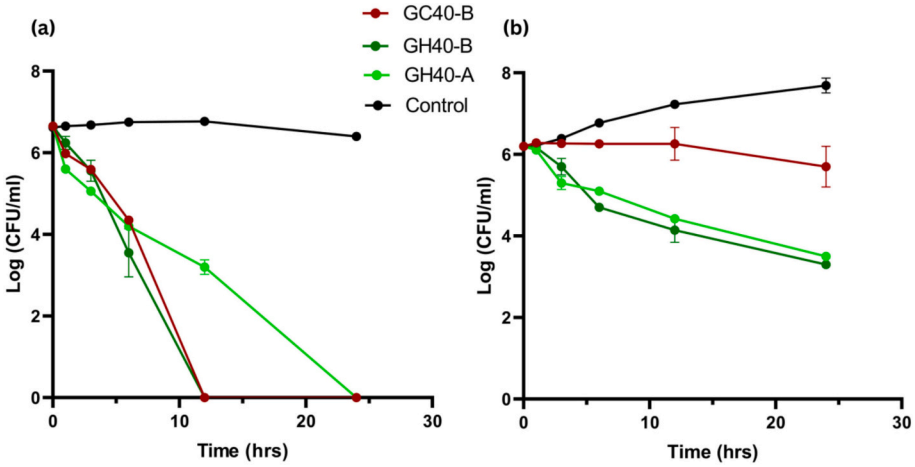

Fig. 14. Time-kill assay of mucoadhesive dental chips against *A. actinomycetemcomitans* (a) and *S. mutans* (b) over 24 h.

accompanied by bulk erosion. This explains the initial burst release and the early loss of matrix integrity observed in the *in vitro* studies. In contrast, CH-based chips (Fig. 12(j,k,l)) retained a compact and continuous architecture after release, displaying only localized surface roughening and controlled exfoliation. This preserved morphology suggested that drug release was governed predominantly by diffusion through a stable polymeric matrix, resulting in sustained release profiles. The observed interactions indicate that these structural disruptions result from polymer swelling, network relaxation [120], and diffusion of nanoparticles from the matrices [121].

The quantitative SEM analysis not only substantiates the visual observations but also provides mechanistic evidence that the observed morphological changes are driven by dynamic pore restructuring. In the CMC-based chips, the initial porosity decreased from 15.53% to 8.17%, following the drug release, while the average pore size increased markedly from 0.068 μm^2 to 0.186 μm^2. Similarly, CH-based chips exhibited a reduction in porosity from 13.07% to 6.16%, accompanied by an increase in pore size from 0.033 μm^2 to 0.103 μm^2. This inverse relationship between porosity and pore size indicates that the release process is associated with pore coalescence, where smaller voids merge into larger channels due to hydration-induced polymer relaxation and matrix erosion. These structural transformations are strongly supported by the swelling and erosion profiles of the chips, confirming that matrix fragmentation is governed by combined swelling–erosion. The GC40-A and GC40-B formulations exhibited significantly higher swelling (~110%) and matrix erosion (~45%), reflecting extensive water uptake and rapid polymer chain relaxation. This high hydration capacity facilitates the formation of a loosely organized gel network, promoting pore expansion and interconnection, which ultimately leads to the formation of larger diffusion pathways. In contrast, GH40-A and GH40-B chips demonstrated comparatively lower swelling and reduced erosion, indicating a more compact and structurally stable matrix. The denser network in CH-based chips is likely attributed to stronger intermolecular interactions, particularly electrostatic and hydrogen bonding within the GEL–CH complex [122], which restricts excessive water penetration and limits pore growth.

3.13. Antibacterial study

The antibacterial activity of the prepared samples was evaluated against *A. actinomycetemcomitans* and *S. mutans* using the agar diffusion method (Table 5). No inhibition zone was observed for the blank GC40 and GH40 chips against either test strain under the present experimental setup. In contrast, the nanoformulation-loaded dental chips (GC40-A, GC40-B, GH40-A, and GH40-B) exhibited clear zones of inhibition surrounding the chips, indicating potent and uniform antibacterial activity (Fig. 13).

In the present study, the antibacterial effect is mainly attributed to CO (Eug), which served as a potent antimicrobial agent [123]. While the inclusion of AP along with CO contributed to improved antibacterial outcomes, confirming a synergistic relationship that has already been established in the literature [47]. This observation is also consistent with a previous study reporting that AP exhibits the synergistic effect in combination with antibiotics to reverse bacterial resistance [124].

The size of the inhibition zones varied among the formulations, suggesting that incorporating bioactive components improved antibacterial efficacy. The pronounced zone of inhibition after 24 h indicated improved suppression of *A. actinomycetemcomitans* growth. In the case of *S. mutans*, all formulations exhibited moderate inhibitory effects. The sustained release profile of Eug and AP further supports the observed biological effects and contributes to the enhanced antimicrobial performance.

Table 5
Zone of inhibition of nanoformulation-loaded dental chips against tested bacterial strains determined by the agar diffusion method.

Dental chips	*S. mutans*	*A. actinomycetemcomitans*
	Zone of inhibition (mm ± SD)	
GC40-A	8.17 ± 0.4	19.58 ± 0.4
GC40-B	8.25 ± 0.6	19.83 ± 1.4
GH40-A	6.63 ± 0.3	18.92 ± 0.9
GH40-B	6.82 ± 0.4	19.92 ± 1.0

It is noteworthy that the minimum inhibitory concentrations (MICs) of Eug and AP against *A. actinomycetemcomitans* and *S. mutans* strains had been previously determined. For Eug, the MIC was 180 μg/mL, while for AP, the MICs were 3.9 μg/mL (NLC-A) and 7.8 μg/mL (NLC-B) [47]. These MIC values have been plotted in the *in vitro* release profile graphs to correlate the released drug concentrations with the antibacterial threshold. As shown in the *in vitro* release data (Fig. 11a, b), the formulations were capable of sustaining drug release at concentrations exceeding the MIC values over the entire study period, thereby ensuring adequate drug availability and maintenance of inhibitory concentrations required for effective antibacterial activity. Additionally, against *A. actinomycetemcomitans*, AP exhibited minimum bactericidal concentration (MBC) values of 15.60 μg/mL (NLC-A) and 31.25 μg/mL (NLC-B) while the MBC of Eug was 720 μg/mL. While in case of *S. mutans*, both formulations exhibited a bacteriostatic effect.

While the agar diffusion assay confirmed the antibacterial potential of the developed formulations, the time-kill assay was performed to further investigate the kinetics and the duration of their antimicrobial activity. Fig. 14 shows the time-kill kinetics of the developed dental chips, revealing a time-dependent inhibition of bacterial growth. Given an initial inoculum of approximately 10^6 CFU/mL, a progressive decrease in CFU was observed after exposure to dental chips. Generally, bactericidal activity is defined as 90% killing at 6 h, equivalent to 99.9% killing at 24 h [125].

After 6 h, a marked reduction in bacterial counts was observed, corresponding to approximately 3 logs reduction, thereby meeting the bactericidal threshold [126]. For up to 24 h, all formulations achieved undetectable bacterial levels, representing a $\geq$ 6-log reduction. These findings demonstrate that all tested mucoadhesive chips possess potent bactericidal activity against *A. actinomycetemcomitans*. However, as shown in Fig. 14b, formulation GC40-B exhibited minimal antibacterial activity against *S. mutans*, with bacterial counts remaining near the initial inoculum throughout the 24 h period. In contrast, GH40-A and GH40-B demonstrated moderate reduction, with counts decreasing to 3.5 and 3.3 log CFU/mL, respectively, by 24 h.

Notably, none of the formulations achieved a $\geq$ 3 $\log_{10}$ CFU/mL reduction (≥99.9% killing) relative to the control, indicating a lack of bactericidal activity under the tested conditions [127]. This observation is in agreement with the literature, where time-kill kinetics analysis has demonstrated that leaf extracts exert a bacteriostatic effect against all tested Gram-negative bacteria [128]. Likewise, carboxymethyl chitosan-based systems inhibit *S. mutans* adherence without exerting direct killing [129], whereas CH-containing chewing gum has been shown to reduce salivary *S. mutans* colony counts [130]. Consistent with these findings, both types of chips demonstrated a bacteriostatic effect against *S. mutans*. However, CH-based chips suppress *S. mutans* growth more effectively than CMC-based chips. This enhanced efficacy may be attributable to the intrinsic antibacterial properties of CH, underscoring its functional advantage over CMC in the developed formulations. Collectively, these outcomes elucidate the antimicrobial efficacy and sustained-release profiles of the developed formulations, demonstrating that the nano-dental chips exert bactericidal activity against *A. actinomycetemcomitans* while exhibiting bacteriostatic activity against *S. mutans*. Such divergent antimicrobial behavior likely arises from species-specific susceptibility or intrinsic variations in cell wall architecture between the two pathogens.

3.14. Stability study

The stability of dental chip formulations was evaluated over six months at 5 °C, 25 °C, and 40 °C. Across all formulations, variations in weight, thickness, surface pH, and solution pH remained generally low. Table 6 summarizes the stability parameters, showing that at 25 °C, all formulations exhibited minimal changes (variations in weight and thickness < 1.5%), with surface and solution pH remaining essentially stable. Elevated temperature (40 °C) produced slightly higher variations in weight and thickness, while pH changes remained minor. Low-temperature storage at 5 °C caused modest changes in weight and slight fluctuations in thickness and pH, most notably in GC40-A and GC40-B.

Based on earlier temperature stability studies that identified 25 °C as the most suitable storage condition, the study was continued for an additional three months to further assess the physical and chemical stability of the formulations. The results demonstrated that drug content uniformity remained within acceptable limits, with Eug content exhibiting values of 94.2 ± 2.2%, and AP content was up to 94.9 ± 0.8%. The detailed parameters evaluated after the 9 months stability study are presented in Table S3. Overall, these findings confirm the stability and robustness of the mucoadhesive dental chip formulations, as all samples preserved their chemical integrity throughout the study period without any detectable degradation products.

Table 6
The findings of stability studies of dental chips after 6 months.

Dental chips	Temperature (°C)	Weight variation (% ± SD)	Thickness variation (% ± SD)	Surface pH variation (% ± SD)	Solution pH variation (% ± SD)
GC40-A	40	2.67 ± 0.74	0.97 ± 0.67	1.45 ± 0.10	0.30 ± 1.90
	25	1.35 ± 0.89	1.25 ± 0.41	0.46 ± 0.52	0.21 ± 0.71
	5	4.86 ± 2.45	1.62 ± 2.63	2.38 ± 3.62	0.28 ± 2.64
GC40-B	40	3.48 ± 3.00	2.56 ± 3.31	1.04 ± 2.47	2.04 ± 0.40
	25	1.15 ± 0.41	1.45 ± 0.35	1.06 ± 1.76	1.00 ± 1.02
	5	2.97 ± 1.84	1.87 ± 1.23	1.44 ± 2.93	1.71 ± 3.56
GH40-A	40	2.03 ± 1.60	0.81 ± 1.08	1.72 ± 2.51	0.30 ± 0.43
	25	1.12 ± 0.21	0.32 ± 1.91	0.41 ± 0.15	0.32 ± 1.32
	5	2.11 ± 0.66	2.33 ± 2.17	1.18 ± 1.41	1.09 ± 2.08
GH40-B	40	2.48 ± 0.73	3.00 ± 1.53	1.78 ± 0.21	2.09 ± 0.30
	25	1.05 ± 0.30	0.78 ± 0.42	0.18 ± 2.12	0.45 ± 0.83
	5	1.76 ± 1.20	1.55 ± 4.11	2.04 ± 2.47	3.06 ± 1.05

4. Conclusion

The present study successfully developed and characterized a biodegradable, nanoloaded dental chip for localized and sustained drug delivery within periodontal pockets. By embedding optimized NLC into GEL matrices blended with CH or CMC, we established a hybrid system combining nanoscale encapsulation with prolonged local residence time. These polymer blends demonstrated excellent film-forming ability, mechanical robustness, and oral pH compatibility. Notably, molecular docking analysis confirmed thermodynamically favorable interactions between the bioactive compounds and the GEL matrices, which directly contributed to structural stability and controlled drug release. Among the formulations, the GEL–CH matrix exhibited the superior profile, balancing the mucoadhesive strength with the controlled release. Dental chips maintained the dimensional uniformity, low residual moisture, and the mechanical resilience required to withstand physiological stresses in the periodontal pocket. Furthermore, robust *in vitro* antibacterial efficacy underscored the system's potential to prevent and manage oral infections. By overcoming the rapid clearance and sub-therapeutic dosing limitations of conventional therapies, this platform offers a highly effective, targeted approach to periodontal care. Moving forward, comprehensive *in vivo* evaluations and clinical validation will be critical to translating these promising material properties into practical therapeutic success.

CRediT authorship contribution statement

Rabia Ashfaq: Writing – review & editing, Writing – original draft, Visualization, Software, Methodology, Investigation, Formal analysis, Data curation, Conceptualization. **Anita Kovács:** Writing – original draft, Methodology, Formal analysis. **Szilvia Berkó:** Writing – original draft, Supervision, Resources, Project administration, Methodology, Investigation, Funding acquisition, Formal analysis. **Gábor Katona:** Writing – original draft, Methodology, Investigation. **Rita Ambrus:** Writing – original draft, Methodology, Investigation. **Tamás F. Polgár:** Visualization, Investigation. **Mária Szécsényi:** Writing – original draft, Methodology, Investigation, Formal analysis. **Katalin Burián:** Writing – original draft, Methodology, Formal analysis. **Mária Budai-Szűcs:** Writing – review & editing, Writing – original draft, Visualization, Supervision, Resources, Project administration, Methodology, Investigation, Funding acquisition, Formal analysis, Data curation, Conceptualization.

Funding information

The University of Szeged Open Access Fund (FundRef, Grant No. 8562) is acknowledged for funding the open access publication.

Project no TKP2021-EGA-32 has been implemented with the support provided by the Ministry of Culture and Innovation of Hungary from the National Research, Development, and Innovation Fund, financed under the TKP2021-EGA funding scheme. This work was supported by the János Bolyai Research Scholarship of the Hungarian Academy of Sciences (M. Budai-Szűcs, BO/00244/24). R.A was supported by University Research Scholarship Program of the Ministry of Culture and Innovation, financed by the National Research, Development, and Innovation Fund (EKÖP-187-SZTE).

Declaration of competing interest

The authors declare no conflicts of interest.

Appendix A. Supplementary data

Supplementary data to this article can be found online at https://doi.org/10.1016/j.bioadv.2026.215007.

Data availability

Data will be made available on request.

References

[1] P.D. Marsh, Dental plaque as a microbial biofilm, Caries Res. 38 (2004) 204–211, https://doi.org/10.1159/000077756.
[2] T.W. MaCfarlane, Plaque-related infections, J. Med. Microbiol. 29 (1989) 161–170, https://doi.org/10.1099/00222615-29-3-161.
[3] R. Ashfaq, B. Sisa, A. Kovács, S. Berkó, M. Szécsényi, K. Burián, P. Vályi, M. Budai-Szűcs, Factorial design of in situ gelling two-compartment systems containing chlorhexidine for the treatment of periodontitis, Eur. J. Pharm. Sci. 191 (2023) 106607, https://doi.org/10.1016/j.ejps.2023.106607.
[4] M.E. Yusoff, D.R.H. Hamdan, P.M.D.H. Taib, D.T.L. Peng, P.D.M. Mohamed, P.M. D.R. Shaari, Overview of Gram-negative anaerobic pathogens associated with

periodontal disease: a review, Asian J. Med. Biomed. 8 (2024) 98–110, https://doi.org/10.37231/ajmb.2024.8.2.761.
[5] S. Cheng, H. Wang, X. Pan, C. Zhang, K. Zhang, Z. Chen, W. Dong, A. Xie, X. Qi, Dendritic hydrogels with robust inherent antibacterial properties for promoting bacteria-infected wound healing, ACS Appl. Mater. Interfaces 14 (2022) 11144–11155, https://doi.org/10.1021/acsami.1c25014.
[6] R. Ashfaq, A. Kovács, S. Berkó, M. Budai-Szűcs, Smart biomaterial gels for periodontal therapy: a novel approach, Biomed. Pharmacother. 183 (2025) 117836, https://doi.org/10.1016/j.biopha.2025.117836.
[7] X. Ge, J. Hu, X. Qi, Y. Shi, X. Chen, Y. Xiang, H. Xu, Y. Li, Y. Zhang, J. Shen, H. Deng, An immunomodulatory hydrogel featuring antibacterial and reactive oxygen species scavenging properties for treating periodontitis in diabetes, Adv. Mater. 37 (2025) 2412240, https://doi.org/10.1002/adma.202412240.
[8] R. Ashfaq, A. Kovács, S. Berkó, M. Budai-Szűcs, Developments in alloplastic bone grafts and barrier membrane biomaterials for periodontal guided tissue and bone regeneration therapy, Int. J. Mol. Sci. 25 (2024) 7746, https://doi.org/10.3390/ijms25147746.
[9] T. Biswal, S.K. BadJena, D. Pradhan, Sustainable biomaterials and their applications: a short review, Mater. Today Proc. 30 (2020) 274–282, https://doi.org/10.1016/j.matpr.2020.01.437.
[10] S. Rawdkuen, A. Faseha, S. Benjakul, P. Kaewprachu, Application of anthocyanin as a color indicator in gelatin films, Food Biosci. 36 (2020) 100603, https://doi.org/10.1016/j.fbio.2020.100603.
[11] C. Qiao, X. Ma, J. Zhang, J. Yao, Molecular interactions in gelatin/chitosan composite films, Food Chem. 235 (2017) 45–50, https://doi.org/10.1016/j.foodchem.2017.05.045.
[12] C. Mu, J. Guo, X. Li, W. Lin, D. Li, Preparation and properties of dialdehyde carboxymethyl cellulose crosslinked gelatin edible films, Food Hydrocoll. 27 (2012) 22–29, https://doi.org/10.1016/j.foodhyd.2011.09.005.
[13] P. Cazón, G. Velazquez, J.A. Ramírez, M. Vázquez, Polysaccharide-based films and coatings for food packaging: a review, Food Hydrocoll. 68 (2017) 136–148, https://doi.org/10.1016/j.foodhyd.2016.09.009.
[14] M. Hadian, S.M.H. Hosseini, A. Farahnaky, G.R. Mesbahi, G.H. Yousefi, A. A. Saboury, Isothermal titration calorimetric and spectroscopic studies of β-lactoglobulin-water-soluble fraction of Persian gum interaction in aqueous solution, Food Hydrocoll. 55 (2016) 108–118, https://doi.org/10.1016/j.foodhyd.2015.11.006.
[15] Protein + polysaccharide coacervates and complexes: from scientific background to their application as functional ingredients in food products, in: Modern Biopolymer Science, Academic Press, 2009, pp. 327–363, https://doi.org/10.1016/B978-0-12-374195-0.00011-2.
[16] X. He, W. Lu, C. Sun, H. Khalesi, A. Mata, R. Andaleeb, Y. Fang, Cellulose and cellulose derivatives: different colloidal states and food-related applications, Carbohydr. Polym. 255 (2021) 117334, https://doi.org/10.1016/j.carbpol.2020.117334.
[17] J.-F. Su, Z. Huang, X.-Y. Yuan, X.-Y. Wang, M. Li, Structure and properties of carboxymethyl cellulose/soy protein isolate blend edible films crosslinked by Maillard reactions, Carbohydr. Polym. 79 (2010) 145–153, https://doi.org/10.1016/j.carbpol.2009.07.035.
[18] N.A. Al-Tayyar, A.M. Youssef, R. Al-hindi, Antimicrobial food packaging based on sustainable bio-based materials for reducing foodborne pathogens: a review, Food Chem. 310 (2020) 125915, https://doi.org/10.1016/j.foodchem.2019.125915.
[19] H. Almasi, B. Ghanbarzadeh, A.A. Entezami, Physicochemical properties of starch–CMC–nanoclay biodegradable films, Int. J. Biol. Macromol. 46 (2010) 1–5, https://doi.org/10.1016/j.ijbiomac.2009.10.001.
[20] M. Yildirim-Yalcin, F. Tornuk, O.S. Toker, Recent advances in the improvement of carboxymethyl cellulose-based edible films, Trends Food Sci. Technol. 129 (2022) 179–193, https://doi.org/10.1016/j.tifs.2022.09.022.
[21] S.-M. Hasheminya, R. Rezaei Mokarram, B. Ghanbarzadeh, H. Hamishekar, H. S. Kafil, Physicochemical, mechanical, optical, microstructural and antimicrobial properties of novel kefiran-carboxymethyl cellulose biocomposite films as influenced by copper oxide nanoparticles (CuONPs), Food Packag. Shelf Life 17 (2018) 196–204, https://doi.org/10.1016/j.fpsl.2018.07.003.
[22] V. Bifani, C. Ramírez, M. Ihl, M. Rubilar, A. García, N. Zaritzky, Effects of murta (*Ugni molinae* Turcz) extract on gas and water vapor permeability of carboxymethylcellulose-based edible films, LWT Food Sci. Technol. 40 (2007) 1473–1481, https://doi.org/10.1016/j.lwt.2006.03.011.
[23] T. Xie, Z. Liao, H. Lei, X. Fang, J. Wang, Q. Zhong, Antibacterial activity of food-grade chitosan against *Vibrio parahaemolyticus* biofilms, Microb. Pathog. 110 (2017) 291–297, https://doi.org/10.1016/j.micpath.2017.07.011.
[24] F.S. Rezaei, F. Sharifianjazi, A. Esmaeilkhanian, E. Salehi, Chitosan films and scaffolds for regenerative medicine applications: a review, Carbohydr. Polym. 273 (2021) 118631, https://doi.org/10.1016/j.carbpol.2021.118631.
[25] T. de Moraes Crizel, A. de Oliveira Rios, V.D. Alves, N. Bandarra, M. Moldão-Martins, S. Hickmann Flôres, Active food packaging prepared with chitosan and olive pomace, Food Hydrocoll. 74 (2018) 139–150, https://doi.org/10.1016/j.foodhyd.2017.08.007.
[26] O. Felt, P. Buri, R. Gurny, Chitosan: a unique polysaccharide for drug delivery, Drug Dev. Ind. Pharm. 24 (1998) 979–993, https://doi.org/10.3109/03639049809089942.
[27] M. Darbasi, G. Askari, H. Kiani, F. Khodaiyan, Development of chitosan based extended-release antioxidant films by control of fabrication variables, Int. J. Biol. Macromol. 104 (2017) 303–310, https://doi.org/10.1016/j.ijbiomac.2017.06.055.
[28] H. Wang, F. Ding, L. Ma, Y. Zhang, Edible films from chitosan-gelatin: physical properties and food packaging application, Food Biosci. 40 (2021) 100871, https://doi.org/10.1016/j.fbio.2020.100871.
[29] M. Aider, Chitosan application for active bio-based films production and potential in the food industry: review, LWT Food Sci. Technol. 43 (2010) 837–842, https://doi.org/10.1016/j.lwt.2010.01.021.
[30] H. Zhang, X. Lin, X. Cao, Y. Wang, J. Wang, Y. Zhao, Developing natural polymers for skin wound healing, Bioact. Mater. 33 (2024) 355–376, https://doi.org/10.1016/j.bioactmat.2023.11.012.
[31] A. Baranwal, A. Kumar, A. Priyadharshini, G.S. Oggu, I. Bhatnagar, A. Srivastava, P. Chandra, Chitosan: an undisputed bio-fabrication material for tissue engineering and bio-sensing applications, Int. J. Biol. Macromol. 110 (2018) 110–123, https://doi.org/10.1016/j.ijbiomac.2018.01.006.
[32] J.T. Martins, M.A. Cerqueira, A.A. Vicente, Influence of α-tocopherol on physicochemical properties of chitosan-based films, Food Hydrocoll. 27 (2012) 220–227, https://doi.org/10.1016/j.foodhyd.2011.06.011.
[33] R. Mohammadi, M.A. Mohammadifar, M. Rouhi, M. Kariminejad, A. M. Mortazavian, E. Sadeghi, S. Hasanvand, Physico-mechanical and structural properties of eggshell membrane gelatin-chitosan blend edible films, Int. J. Biol. Macromol. 107 (2018) 406–412, https://doi.org/10.1016/j.ijbiomac.2017.09.003.
[34] H. Wen, D. Tang, Y. Lin, J. Zou, Z. Liu, P. Zhou, X. Wang, Enhancement of water barrier and antimicrobial properties of chitosan/gelatin films by hydrophobic deep eutectic solvent, Carbohydr. Polym. 303 (2023) 120435, https://doi.org/10.1016/j.carbpol.2022.120435.
[35] C. Zhang, Z. Yang, J. Shi, X. Zou, X. Zhai, X. Huang, Z. Li, M. Holmes, M. Daglia, J. Xiao, Physical properties and bioactivities of chitosan/gelatin-based films loaded with tannic acid and its application on the preservation of fresh-cut apples, LWT 144 (2021) 111223, https://doi.org/10.1016/j.lwt.2021.111223.
[36] Chitosan-based biodegradable dental chips impregnated with chlorhexidine gluconate for the treatment of periodontitis, RSC Pharm. 2 (2025) 1580–1592, https://doi.org/10.1039/d5pm00086f.
[37] U. Sankararajan, BeethaRohini, Nithyapriya, Sasidharan, Formulation and evaluation of ciprofloxacin dental films for periodontitis, J. Chem. Pharm. Res. 4 (2012) 2964–2971.
[38] B.N. Vandekerckhove, M. Quirynen, D. van Steenberghe, The use of tetracycline-containing controlled-release fibers in the treatment of refractory periodontitis, J. Periodontol. 68 (1997) 353–361, https://doi.org/10.1902/jop.1997.68.4.353.
[39] R. Elkayam, M. Friedman, A. Stabholz, A.W. Soskolne, M.N. Sela, L. Golub, Sustained release device containing minocycline for local treatment of periodontal disease, J. Control. Release 7 (1988) 231–236, https://doi.org/10.1016/0168-3659(88)90055-7.
[40] S. Asghar, I.U. Khan, S. Salman, S.H. Khalid, R. Ashfaq, T.F. Vandamme, Plant-derived nanotherapeutic systems to counter the overgrowing threat of resistant microbes and biofilms, Adv. Drug Deliv. Rev. 179 (2021) 114019, https://doi.org/10.1016/j.addr.2021.114019.
[41] M. Ulanowska, B. Olas, M. Ulanowska, B. Olas, Biological properties and prospects for the application of eugenol—a review, Int. J. Mol. Sci. 22 (2021), https://doi.org/10.3390/ijms22073671.
[42] P. Suttiarporn, T. Taithaisong, S. Namkhot, S. Luangkamin, P. Suttiarporn, T. Taithaisong, S. Namkhot, S. Luangkamin, Enhanced eugenol composition in clove essential oil by deep eutectic solvent-based ultrasonic extraction and microwave-assisted hydrodistillation, Molecules 30 (2025), https://doi.org/10.3390/molecules30030504.
[43] Z. Mushtaq, N.B. Sadeer, M. Hussain, Mahwish, S.A. Alsagaby, M. Imran, T. Mumtaz, M. Umar, A. Tauseef, W. Al Abdulmonem, T. Tufail, E. Al Jbawi, M. F. Mahomoodally, Therapeutical properties of apigenin: a review on the experimental evidence and basic mechanisms, Int. J. Food Prop. 26 (2023) 1914–1939, https://doi.org/10.1080/10942912.2023.2236329.
[44] J. Madunić, I.V. Madunić, G. Gajski, J. Popić, V. Garaj-Vrhovac, Apigenin: a dietary flavonoid with diverse anticancer properties, Cancer Lett. 413 (2018) 11–22, https://doi.org/10.1016/j.canlet.2017.10.041.
[45] S. Khan, A. Sharma, Jain, An Overview of Nanostructured Lipid Carriers and Its Application in Drug Delivery Through Different Routes, 2022, https://doi.org/10.34172/apb.2023.056.
[46] R. Ashfaq, A. Rasul, S. Asghar, A. Kovács, S. Berkó, M. Budai-Szűcs, Lipid nanoparticles: an effective tool to improve the bioavailability of nutraceuticals, Int. J. Mol. Sci. 24 (2023) 15764, https://doi.org/10.3390/ijms242115764.
[47] R. Ashfaq, A. Kovács, S. Berkó, G. Katona, D. Paróczai, M. Szécsényi, K. Burián, P. Vályi, K. Veres, G. Girst, A. Hunyadi, T.F. Polgár, M. Budai-Szűcs, Co-encapsulated apigenin and clove oil in nanostructured lipid carriers for enhanced periodontal disease therapy, J. Drug Deliv. Sci. Technol. 115 (2026) 107644, https://doi.org/10.1016/j.jddst.2025.107644.
[48] R.N. Sahoo, S. Pattanaik, G. Pattnaik, S. Mallick, R. Mohapatra, Review on the use of molecular docking as the first line tool in drug discovery and development, Indian J. Pharm. Sci. 84 (2022) 1334–1337, https://doi.org/10.36468/pharmaceutical-sciences.1031.
[49] S. Talluri, Molecular docking and virtual screening based prediction of drugs for COVID-19, Comb. Chem. High Throughput Screen. 24 (2021) 716–728, https://doi.org/10.2174/1386207323666200814132149.
[50] K. Chaudhary, N. Mishra, A review on molecular docking: novel tool for drug discovery, JSM Chem. 4 (2016) 1029.
[51] PubChem, PubChem, (n.d.). https://pubchem.ncbi.nlm.nih.gov/ (accessed January 15, 2026).
[52] G. Hutchison, Avogadro 1.2 Released, Avogadro. https://avogadro.cc/news/avogadro-1-2-0-released/, 2016. (Accessed 15 January 2026).

[53] Downloads – PyRx – Python Prescription, (n.d.). https://pyrx.sourceforge.io/downloads/ (accessed January 15, 2026).
[54] D. Systèmes, Free Download: BIOVIA Discovery Studio Visualizer, Dassault Systèmes. https://discover.3ds.com/discovery-studio-visualizer-download, 2020. (Accessed 15 January 2026).
[55] A. Varela-Garcia, J.L. Gomez-Amoza, A. Concheiro, C. Alvarez-Lorenzo, Imprinted contact lenses for ocular administration of antiviral drugs, Polymers 12 (2020) 2026, https://doi.org/10.3390/polym12092026.
[56] S. Kumar, A. Shukla, P.P. Baul, A. Mitra, D. Halder, Biodegradable hybrid nanocomposites of chitosan/gelatin and silver nanoparticles for active food packaging applications, Food Packag. Shelf Life 16 (2018) 178–184, https://doi.org/10.1016/j.fpsl.2018.03.008.
[57] S. Parveen, S. Nazeer, G.A. Chotana, A. Kanwal, B. Batool, N. Bukhari, A. Yaqoob, F. Talib, Designing of chitosan/gelatin based nanocomposite films integrated with *Vachellia nilotica* gum carbon dots for smart food packaging applications, Int. J. Biol. Macromol. 264 (2024) 130208, https://doi.org/10.1016/j.ijbiomac.2024.130208.
[58] A. Khan, P. Ezati, J.-W. Rhim, Chitosan/gelatin-based multifunctional film integrated with green tea carbon dots to extend the shelf life of pork, Food Packag. Shelf Life 37 (2023) 101075, https://doi.org/10.1016/j.fpsl.2023.101075.
[59] P. Kraisit, S. Limmatvapirat, M. Luangtana-Anan, P. Sriamornsak, Buccal administration of mucoadhesive blend films saturated with propranolol loaded nanoparticles, Asian J. Pharm. Sci. 13 (2018) 34–43, https://doi.org/10.1016/j.ajps.2017.07.006.
[60] S. Salehi, S. Boddohi, New formulation and approach for mucoadhesive buccal film of rizatriptan benzoate, Prog. Biomater. 6 (2017) 175–187, https://doi.org/10.1007/s40204-017-0077-7.
[61] F. Mussa, H. Mousi, M. Treki, The use of chitosan in the preparation of bioadhesive buccal films: film-forming ability and sustaining ibuprofen release, Libyan Int. Med. Univ. J. 06 (2021) 91–98, https://doi.org/10.4103/liuj.liuj_78_21.
[62] The role of coatings and contact angle measurements on biomedical devices, (n.d.). https://www.biolinscientific.com/blog/enhancing-biomedical-devices-the-role-of-coatings-and-contact-angle-measurements (accessed January 13, 2026).
[63] K. Ludasi, A. Sass, K. Kristó, A. Kelemen, K. Pintye-Hódi, T. Sovány, Behavior of aqueous medicated inks on porous tablet surfaces, Pharmaceutics 17 (2025) 908, https://doi.org/10.3390/pharmaceutics17070908.
[64] N. Kis, A. Kovács, M. Budai-Szűcs, A. Gácsi, E. Csányi, I. Csóka, S. Berkó, Investigation of silicone-containing semisolid in situ film-forming systems using QbD tools, Pharmaceutics 11 (2019) 660, https://doi.org/10.3390/pharmaceutics11120660.
[65] T.A. Professionals, Stable Micro Systems will no longer be posting to this blog, visit our new blog on our main website.: Texture Analysis in Action: the Film Support Rig, Stable Micro Systems Will No Longer Be Posting to This Blog, Visit Our New Blog on Our Main Website. https://textureanalysisprofessionals.blogspot.com/2015/02/texture-analysis-in-action-film-support.html, 2015. (Accessed 16 December 2025).
[66] B. Li, J. Wang, Q. Gui, H. Yang, Drug-loaded chitosan film prepared via facile solution casting and air-drying of plain water-based chitosan solution for ocular drug delivery, Bioact. Mater. 5 (2020) 577–583, https://doi.org/10.1016/j.bioactmat.2020.04.013.
[67] M.R. Akram, M. Ahmad, A. Abrar, R.M. Sarfraz, A. Mahmood, Formulation design and development of matrix diffusion controlled transdermal drug delivery of glimepiride, Drug Des. Dev. Ther. 12 (2018) 349–364, https://doi.org/10.2147/DDDT.S147082.
[68] M.D. Arpa, M.Z. Ünükür, Ü.C. Erim, Formulation, characterization and in vitro release studies of terbinafine hydrochloride loaded buccal films, J. Res. Pharm. 25 (2025) 667–680.
[69] E.M. Nour, S.E. El-Habashy, M.G. Shehat, M.M. Essawy, R.M. El-Moslemany, N. M. Khalafallah, Atorvastatin liposomes in a 3D-printed polymer film: a repurposing approach for local treatment of oral candidiasis, Drug Deliv. Transl. Res. 13 (2023) 2847–2868, https://doi.org/10.1007/s13346-023-01353-4.
[70] J. Schindelin, I. Arganda-Carreras, E. Frise, V. Kaynig, M. Longair, T. Pietzsch, S. Preibisch, C. Rueden, S. Saalfeld, B. Schmid, J.-Y. Tinevez, D.J. White, V. Hartenstein, K. Eliceiri, P. Tomancak, A. Cardona, Fiji: an open-source platform for biological-image analysis, Nat. Methods 9 (2012) 676–682, https://doi.org/10.1038/nmeth.2019.
[71] W. Khunawattanakul, T. Pongjanyakul, Chitosan−magnesium aluminum silicate nanocomposite−based films of nicotine for buccal delivery: mixing order effect and drug retention, J. Drug Deliv. Sci. Technol. 92 (2024) 105266, https://doi.org/10.1016/j.jddst.2023.105266.
[72] S.-M. Yun, M.-H. Lee, K.-J. Lee, H.-O. Ku, S.-W. Son, Y.-S. Joo, Quantitative analysis of eugenol in clove extract by a validated HPLC method, J. AOAC Int. 93 (2010) 1806–1810.
[73] K. Khosravinia, A. Kiani, Protocol for fabricating pseudocapacitor electrodes using ultra-short laser pulses for *in situ* nanostructure generation, STAR Protoc. 4 (2023) 102469, https://doi.org/10.1016/j.xpro.2023.102469.
[74] A.S. Azizo, M.D.H. Wirzal, M.R. Bilad, A.R.M. Yusoff, Assessment of nylon 6, 6 nanofibre membrane for microalgae harvesting, AIP Conf. Proc. 1891 (2017) 020032, https://doi.org/10.1063/1.5005365.
[75] G.A. Filipe, V.A.I. Silveira, M.C. Gonçalves, R.R. Beltrame Machado, C. V. Nakamura, C. Baldo, S. Mali, R.K.T. Kobayashi, M.A.P. Colabone Celligoi, Bioactive films for the control of skin pathogens with sophorolipids from Starmerella bombicola, Polym. Bull. 80 (2023) 10809–10823, https://doi.org/10.1007/s00289-022-04575-7.
[76] B. Azamatov, A. Dzhes, A. Borisov, D. Kaliyev, B. Maratuly, A. Sagidugumar, M. Alexandr, A. Turlybekuly, S. Plotnikov, Antibacterial properties of copper-tantalum thin films: the impact of copper content and thermal treatment on implant coatings, Heliyon 11 (2025) e41130, https://doi.org/10.1016/j.heliyon.2024.e41130.
[77] M.D. Arpa, N.Ü. Okur, M.K. Gök, S. Özgümüş, E. Cevher, Chitosan-based buccal mucoadhesive patches to enhance the systemic bioavailability of tizanidine, Int. J. Pharm. 642 (2023) 123168, https://doi.org/10.1016/j.ijpharm.2023.123168.
[78] H. Ej, S. Ak, W. J, K. Dr, N. Mt, Effect of glycerol on the physicochemical properties of films based on legume protein concentrates: a comparative study, J. Texture Stud. 50 (2019), https://doi.org/10.1111/jtxs.12460.
[79] J. Tarique, S.M. Sapuan, A. Khalina, Effect of glycerol plasticizer loading on the physical, mechanical, thermal, and barrier properties of arrowroot (Maranta arundinacea) starch biopolymers, Sci. Rep. 11 (2021) 13900, https://doi.org/10.1038/s41598-021-93094-y.
[80] G. Abera, B. Woldeyes, H.D. Demash, G. Miyake, The effect of plasticizers on thermoplastic starch films developed from the indigenous Ethiopian tuber crop Anchote (*Coccinia abyssinica*) starch, Int. J. Biol. Macromol. 155 (2020) 581–587, https://doi.org/10.1016/j.ijbiomac.2020.03.218.
[81] D. Putri, R. Dwiastuti, M. Hadimartono, A. Nugroho, Optimization of mixing temperature and sonication duration in liposome preparation, J. Pharm. Sci. Community 14 (2017) 79–85, https://doi.org/10.24071/jpsc.142728.
[82] S. Honary, F. Zahir, Effect of zeta potential on the properties of nano-drug delivery systems - a review (part 2), Trop. J. Pharm. Res. 12 (2013) 265–273, https://doi.org/10.4314/tjpr.v12i2.20.
[83] What is Transmission Electron Microscopy? TEM Principles & More, (n.d.). https://www.jeolusa.com/RESOURCES/Electron-Optics/transmission-electron-microscopy (accessed January 14, 2026).
[84] R. Ashfaq, T. Nora, A. Kovács, S. Berkó, G. Katona, R. Ambrus, T. Ferenc Polgár, K. Burián, M. Szécsényi, M. Budai-Szucs, Hydrogel–Nanolipid Formulations for the Complex Anti-Inflammatory and Antimicrobial Therapy of Periodontitis, 2025. https://www.mdpi.com/1999-4923/17/5/620. (Accessed 14 June 2025).
[85] P.C. Agu, C.A. Afiukwa, O.U. Orji, E.M. Ezeh, I.H. Ofoke, C.O. Ogbu, E.I. Ugwuja, P.M. Aja, Molecular docking as a tool for the discovery of molecular targets of nutraceuticals in diseases management, Sci. Rep. 13 (2023) 13398, https://doi.org/10.1038/s41598-023-40160-2.
[86] J. Li, C.-Z. Li, C. Shi, J. Aliakbarlu, H. Cui, L. Lin, Antibacterial mechanisms of clove essential oil against Staphylococcus aureus and its application in pork, Int. J. Food Microbiol. 380 (2022) 109864, https://doi.org/10.1016/j.ijfoodmicro.2022.109864.
[87] J. Li, Y. Zhao, Y. Zhang, C. Nardin, Core-shell gelatin-chitosan nanoparticles with lysozyme responsiveness formed via pH-drive and transglutaminase cross-linking, Int. J. Biol. Macromol. 292 (2025) 138802, https://doi.org/10.1016/j.ijbiomac.2024.138802.
[88] S. Bhatia, A. Al-Harrasi, I.H. Almohana, M.S. Albayati, M. Jawad, Y.A. Shah, S. Ullah, A.K. Philip, S.A. Halim, A. Khan, M.K. Anwer, E. Koca, L.Y. Aydemir, S. Dıblan, The physicochemical properties and molecular docking study of plasticized amphotericin B loaded sodium alginate, carboxymethyl cellulose, and gelatin-based films, Heliyon 10 (2024) e24210, https://doi.org/10.1016/j.heliyon.2024.e24210.
[89] Toshi Mayuri Prasad, Rajat Sehgal, Manisha Mallik, Aaysha Tabinda Nabi, Periodontal Disease and Salivary pH: Case Control Study, 2019.
[90] P.-C. Chang, Y.-C. Chao, M.-H. Hsiao, H.-S. Chou, Y.-H. Jheng, X.-H. Yu, N. Lee, C. Yang, D.-M. Liu, Inhibition of periodontitis induction using a stimuli-responsive hydrogel carrying naringin, J. Periodontol. 88 (2017) 190–196, https://doi.org/10.1902/jop.2016.160189.
[91] F. Mussa, H. Mousi, M. Treki, The use of chitosan in the preparation of bioadhesive buccal films: film-forming ability and sustaining ibuprofen release, Libyan Int. Med. Univ. J. 06 (2021) 91–98, https://doi.org/10.4103/liuj.liuj_78_21.
[92] L. Atarés, C. De Jesús, P. Talens, A. Chiralt, Characterization of SPI-based edible films incorporated with cinnamon or ginger essential oils, J. Food Eng. 99 (2010) 384–391, https://doi.org/10.1016/j.jfoodeng.2010.03.004.
[93] L.C. Bertan, P.S. Tanada-Palmu, A.C. Siani, C.R.F. Grosso, Effect of fatty acids and 'Brazilian elemi' on composite films based on gelatin, Food Hydrocoll. 19 (2005) 73–82, https://doi.org/10.1016/j.foodhyd.2004.04.017.
[94] T.h. Shellhammer, J.m. Krochta, Whey protein emulsion film performance as affected by lipid type and amount, J. Food Sci. 62 (1997) 390–394, https://doi.org/10.1111/j.1365-2621.1997.tb04008.x.
[95] N. Gontard, C. Duchez, J.-L. Cuq, S. Guilbert, Edible composite films of wheat gluten and lipids: water vapour permeability and other physical properties, Int. J. Food Sci. Technol. 29 (1994) 39–50, https://doi.org/10.1111/j.1365-2621.1994.tb02045.x.
[96] S. Rbihi, A. Aboulouard, L. Laallam, A. Jouaiti, Contact angle measurements of cellulose based thin film composites: wettability, surface free energy and surface hardness, Surf. Interfaces 21 (2020) 100708, https://doi.org/10.1016/j.surfin.2020.100708.
[97] S.M. Ojagh, M. Rezaei, S.H. Razavi, S.M.H. Hosseini, Development and evaluation of a novel biodegradable film made from chitosan and cinnamon essential oil with low affinity toward water, Food Chem. 122 (2010) 161–166, https://doi.org/10.1016/j.foodchem.2010.02.033.
[98] S.M.B. Hashemi, D. Khodaei, Basil seed gum edible films incorporated with Artemisia sieberi and Achillea santolina essential oils: physical, antibacterial, and antioxidant properties, J. Food Process. Preserv. 45 (2021) e15645, https://doi.org/10.1111/jfpp.15645.

[99] K. Olechno, J. Higuchi, K. Winnicka, Why does mucoadhesion matter? Mucoadhesive drug delivery systems with antifungal activity in the local treatment of oral cavity candidiasis, Materials 19 (2026) 33, https://doi.org/10.3390/ma19010033.
[100] H. Gholizadeh, E. Messerotti, M. Pozzoli, S. Cheng, D. Traini, P. Young, A. Kourmatzis, C. Caramella, H.X. Ong, Application of a thermosensitive in situ gel of chitosan-based nasal spray loaded with tranexamic acid for localised treatment of nasal wounds, AAPS PharmSciTech 20 (2019) 299, https://doi.org/10.1208/s12249-019-1517-6.
[101] S. Mansuri, P. Kesharwani, K. Jain, R.K. Tekade, N.K. Jain, Mucoadhesion: a promising approach in drug delivery system, React. Funct. Polym. 100 (2016) 151–172, https://doi.org/10.1016/j.reactfunctpolym.2016.01.011.
[102] A.B. Nair, R. Kumria, S. Harsha, M. Attimarad, B.E. Al-Dhubiab, I.A. Alhaider, *In vitro* techniques to evaluate buccal films, J. Control. Release 166 (2013) 10–21, https://doi.org/10.1016/j.jconrel.2012.11.019.
[103] P. Kraisit, S. Limmatvapirat, M. Luangtana-Anan, P. Sriamornsak, Buccal administration of mucoadhesive blend films saturated with propranolol loaded nanoparticles, Asian J. Pharm. Sci. 13 (2018) 34–43, https://doi.org/10.1016/j.ajps.2017.07.006.
[104] C. Corredor, T. Teslova, M.V. Cañamares, Z. Chen, J. Zhang, J.R. Lombardi, M. Leona, Raman and surface-enhanced Raman spectra of chrysin, apigenin and luteolin, Vib. Spectrosc. 49 (2009) 190–195, https://doi.org/10.1016/j.vibspec.2008.07.012.
[105] D. Yuan, Z. Wang, B. Li, X. Li, Y. Wang, X. Wang, J. Cao, Y. Guo, H. Du, S. Lu, Complexation of apigenin and oxymatrine leading to enhanced anti-inflammatory activity, J. Nat. Prod. 86 (2023) 1179–1188, https://doi.org/10.1021/acs.jnatprod.2c00947.
[106] P. Larkin, Infrared and Raman Spectroscopy: Principles and Spectral Interpretation, Elsevier, 2017.
[107] P. Vargas Jentzsch, F. Gualpa, L.A. Ramos, V. Ciobotă, Adulteration of clove essential oil: detection using a handheld Raman spectrometer, Flavour Fragr. J. 33 (2018) 184–190, https://doi.org/10.1002/ffj.3438.
[108] Skewness - Measures and Interpretation, GeeksforGeeks (09:53:04+00:00), 2025. https://www.geeksforgeeks.org/data-science/skewness-measures-and-interpretation/. (Accessed 17 May 2026).
[109] A. Tascón, Influence of particle size distribution skewness on dust explosibility, Powder Technol. 338 (2018) 438–445, https://doi.org/10.1016/j.powtec.2018.07.044.
[110] L.T. DeCarlo, On the meaning and use of kurtosis, Psychol. Methods 2 (1997) 292–307, https://doi.org/10.1037/1082-989X.2.3.292.
[111] E.D. Seletchi, O.G. Duliu, Image Processing and Data Analysis in Computed Tomography, September 12, 2006, 2006.
[112] Diff for "FAQ/Simon" - CBU statistics Wiki, (n.d.). https://lsr-wiki-01.mrc-cbu.cam.ac.uk/statswiki/FAQ/Simon?action=diff&rev1=44&rev2=45 (accessed May 17, 2026).
[113] E.S. Yayla, Dikkat eksikliği hiperaktivite bozukluğu ve otizm spektrum bozukluğu tanılı çocukların ebeveynlerinin tutum farklılığının incelenmesi. https://hdl.handle.net/11363/4347, 2022. (Accessed 17 May 2026).
[114] A. Gordillo-Galeano, C.E. Mora-Huertas, Solid lipid nanoparticles and nanostructured lipid carriers: a review emphasizing on particle structure and drug release, Eur. J. Pharm. Biopharm. 133 (2018) 285–308, https://doi.org/10.1016/j.ejpb.2018.10.017.
[115] J. Luan, D. Zhang, L. Hao, C. Li, L. Qi, H. Guo, X. Liu, Q. Zhang, Design and characterization of Amoitone B-loaded nanostructured lipid carriers for controlled drug release, Drug Deliv. 20 (2013) 324–330, https://doi.org/10.3109/10717544.2013.835007.
[116] P. Sodata, S. Duangjit, N. Sarisuta, P. Kraisit, Optimization of mucoadhesive film reinforced with functionalized nanostructured lipid carriers (NLCs) for enhanced triamcinolone acetonide delivery via buccal administration: a Box–Behnken design approach, Sci 7 (2025), https://doi.org/10.3390/sci7010022.
[117] S. Kumar, A. Shukla, P.P. Baul, A. Mitra, D. Halder, Biodegradable hybrid nanocomposites of chitosan/gelatin and silver nanoparticles for active food packaging applications, Food Packag. Shelf Life 16 (2018) 178–184, https://doi.org/10.1016/j.fpsl.2018.03.008.
[118] K. Ghosal, A. Chandra, P. G., S. S., S. Roy, C. Agatemor, S. Thomas, I. Provaznik, Electrospinning over solvent casting: tuning of mechanical properties of membranes, Sci. Rep. 8 (2018) 5058, https://doi.org/10.1038/s41598-018-23378-3.
[119] M.R. Akram, M. Ahmad, A. Abrar, R.M. Sarfraz, A. Mahmood, Formulation design and development of matrix diffusion controlled transdermal drug delivery of glimepiride, Drug Des. Dev. Ther. 12 (2018) 349, https://doi.org/10.2147/DDDT.S147082.
[120] P.L. Ritger, N.A. Peppas, A simple equation for description of solute release II. Fickian and anomalous release from swellable devices, J. Control. Release 5 (1987) 37–42, https://doi.org/10.1016/0168-3659(87)90035-6.
[121] Y. Soleimanian, S.A.H. Goli, J. Varshosaz, L. Di Cesare Mannelli, C. Ghelardini, M. Cirri, F. Maestrelli, β-Sitosterol loaded nanostructured lipid carrier: physical and oxidative stability, in vitro simulated digestion and hypocholesterolemic activity, Pharmaceutics 12 (2020) 386, https://doi.org/10.3390/pharmaceutics12040386.
[122] M. Pereda, A.G. Ponce, N.E. Marcovich, R.A. Ruseckaite, J.F. Martucci, Chitosan-gelatin composites and bi-layer films with potential antimicrobial activity, Food Hydrocoll. 25 (2011) 1372–1381, https://doi.org/10.1016/j.foodhyd.2011.01.001.
[123] H. Cui, C. Zhao, L. Lin, The specific antibacterial activity of liposome-encapsulated *Clove* oil and its application in tofu, Food Control 56 (2015) 128–134, https://doi.org/10.1016/j.foodcont.2015.03.026.
[124] K. Akilandeswari, K. Ruckmani, Synergistic antibacterial effect of apigenin with I^2-lactam antibiotics and modulation of bacterial resistance by a possible membrane effect against methicillin resistant *Staphylococcus aureus*, Cell. Mol. Biol. (Noisy-Le-Grand) 62 (2016) 74–82, doi:10.14715/cmb/.
[125] M. Balouiri, M. Sadiki, S.K. Ibnsouda, Methods for *in vitro* evaluating antimicrobial activity: a review, J. Pharm. Anal. 6 (2016) 71–79, https://doi.org/10.1016/j.jpha.2015.11.005.
[126] Time-Kill Kinetics Assay - Emery Pharma, (n.d.). https://emerypharma.com/solutions/cell-microbiology-services/time-kill-kinetics-assay/ (accessed June 2, 2026).
[127] O. Srichaiyapol, S. Thammawithan, P. Siritongsuk, S. Nasompag, S. Daduang, S. Klaynongsruang, S. Kulchat, R. Patramanon, Tannic Acid-Stabilized Silver Nanoparticles Used in Biomedical Application as an Effective Antimelioidosis and Prolonged Efflux Pump Inhibitor against Melioidosis Causative Pathogen, Molecules 26 (4) (2021) 1004, https://doi.org/10.3390/molecules26041004.
[128] M.N. Donkor, R. Mosobil, J. Abugri, A.-M. Donkor, Antibacterial activities and time-kill analysis of leaf extracts of *Combretum adenogonium* Steud. ex A. Rich in vitro, Biomed. Res. Int. 2025 (2025) 3097612, https://doi.org/10.1155/bmri/3097612.
[129] J. He, Y. Bao, J. Li, Z. Qiu, Y. Liu, X. Zhang, Nanocomplexes of carboxymethyl chitosan/amorphous calcium phosphate reduce oral bacteria adherence and biofilm formation on human enamel surface, J. Dent. 80 (2019) 15–22, https://doi.org/10.1016/j.jdent.2018.11.003.
[130] Z. Khamverdi, F. Farhadian, S. Khazaei, M. Adabi, Efficacy of chitosan-based chewing gum on reducing salivary S. mutans counts and salivary pH: a randomised clinical trial, Acta Odontol. Scand. 79 (2021) 268–274, https://doi.org/10.1080/00016357.2020.1836392.